DE GRUYTER Nanophotonics 2020; 9(7): 1901–1920

Review

Yuyu Li, Khwanchai Tantiwanichapan, Anna K. Swan and Roberto Paiella*

Graphene plasmonic devices for terahertz optoelectronics

https://doi.org/10.1515/nanoph-2020-0211
Received March 26, 2020; accepted April 3, 2020

Abstract: Plasmonic excitations, consisting of collective oscillations of the electron gas in a conductive film or nanostructure coupled to electromagnetic fields, play a prominent role in photonics and optoelectronics. While traditional plasmonic systems are based on noble metals, recent work has established graphene as a uniquely suited materials platform for plasmonic science and applications due to several distinctive properties. Graphene plasmonic oscillations exhibit particularly strong sub-wavelength confinement, can be tuned dynamically through the application of a gate voltage, and span a portion of the infrared spectrum (including mid-infrared and terahertz (THz) wavelengths) that is not directly accessible with noble metals. These properties have been studied in extensive theoretical and experimental work over the past decade, and more recently various device applications are also beginning to be explored. This review article is focused on graphene plasmonic nanostructures designed to address a key outstanding challenge of modern-day optoelectronics – the limited availability of practical, high-performance THz devices. Graphene plasmons can be used as a means to enhance light–matter interactions at THz wavelengths in a highly tunable fashion, particularly through the integration of graphene resonant structures with additional nanophotonic elements. This capability is ideally suited to the development of THz optical modulators (where absorption is switched on and off by tuning the plasmonic resonance) and photodetectors (relying on plasmon-enhanced intraband absorption or rectification of charge-density waves), and promising devices based on these principles have already been reported. Novel radiation mechanisms, including light emission from electrically excited graphene plasmons, are also being explored for the development of compact narrowband THz sources.

Keywords: graphene; hot-carrier effects; plasmonics; terahertz optoelectronics.

1 Introduction

The terahertz (THz) spectral region, often defined as the frequency range between 300 GHz and 10 THz (i. e., the wavelength range between 1 mm and 30 μm), is still largely underutilized due to the relatively low maturity level of relevant components and systems [1–3]. At the same time, the potential of THz technologies for many sensing, spectroscopy, and imaging applications is now well established, and is driving rapid growth in related research and development efforts. These applications rely on the unique ability of THz radiation to penetrate through common packaging materials with little attenuation, and to accurately detect many molecules of interest based on distinctive rotational/vibrational resonances at THz frequencies. Specific areas where these capabilities can play an enabling role [3–5] include security screening (e. g., for the detection of drugs and explosives), medical diagnostics (e. g., for cancer and dental tissue imaging), manufacturing quality control (e. g., in the pharmaceutical, electronics, and aeronautics sectors), as well as fundamental research in condensed-matter physics, chemistry, and astronomy.

Despite significant recent progress, the key challenge limiting the widespread adoption of these technologies remains the development of practical THz optoelectronic devices, especially radiation sources. It is well known that, while the THz spectral region lies at the boundary between the traditional domains of photonics and microwave electronics, device concepts borrowed from either discipline cannot be readily extended to THz frequencies. In

---

Current address: National Electronics and Computer Technology Center, 112 Thailand Science Park, Pathumthani, 12120, Thailand.

***Corresponding author: Roberto Paiella**, Department of Electrical and Computer Engineering and Photonics Center, Boston University, 8 Saint Mary's Street, 02215, Boston, MA, USA,
E-mail: rpaiella@bu.edu. https://orcid.org/0000-0002-7183-6249
Yuyu Li, Khwanchai Tantiwanichapan and Anna K. Swan: Department of Electrical and Computer Engineering and Photonics Center, Boston University, 8 Saint Mary's Street, 02215, Boston, MA, USA,
E-mail: yl@bu.edu (Y. Li), khwan@bu.edu (K. Tantiwanichapan), swan@bu.edu (A.K. Swan)

particular, microwave sources are generally restricted to operation frequencies below ~ 1 THz, due to fundamental materials limitations of traditional semiconductors such as low room-temperature mobilities and small saturation velocities [1]. On the photonics side, THz quantum cascade lasers (QCLs) based on GaAs quantum wells can provide relatively good performance in many respects [6]. However, their spectral coverage is restricted to a limited portion of the THz spectrum (currently 1.2–5.4 THz) due to strong lattice absorption at frequencies within and near the reststrahlen band of GaAs [7]. Additionally, their operation is fundamentally limited to temperatures below ~200 K, so that cryogenic cooling is generally required for high-performance operation, which strongly degrades their portability and integration in practical systems [7]. At present, most THz imaging and spectroscopy systems (including commercial units) rely instead on photoconductive antennas for THz wave generation [8]. However, the operation of these devices requires an ultrafast laser source (typically Ti:sapphire or fiber based), which also significantly increases their size, cost, complexity, and power consumption.

Graphene is a relatively new materials system for THz optoelectronics, but has already received significant attention due to several distinctive properties [9–12]. First, the gapless and linear energy dispersion of its band structure produces a frequency-independent interband absorption spectrum that extends across the entire infrared range. Theoretical studies have also suggested that the same band structure can potentially support population inversion and optical gain at THz frequencies under external carrier injection [13–15], depending on the detailed interplay of the intraband and interband relaxation dynamics. Second, graphene can feature ballistic electronic transport over µm-scale distances with record large room-temperature mobilities [16–19], and thus is an ideal materials system for THz sources based on high-frequency coherent carrier dynamics [20] and electron-beam radiation mechanisms [21–23]. Third, the collective oscillations of the graphene electron (or hole) gas can produce plasmonic resonances at THz or mid-infrared frequencies, as opposed to the visible or near-infrared excitations of traditional plasmonic nanostructures based on noble metals [10, 24–27]. These graphene plasmon polaritons (GPPs) can also feature particularly strong sub-wavelength field confinement and large propagation lengths. Furthermore, they are actively tunable through the use of a gate voltage to control the carrier density, which is particularly attractive for optoelectronic device applications and may open up new opportunities in meta-photonics and transformation optics [28]. Finally, graphene and related van der Waals heterostructures can be readily assembled on any desired substrate (including Si-based microelectronics chips) using well-established aligned transfer techniques [29]. This property (while not specific to THz devices) allows for large-scale system integration, with great potential benefits in terms of system miniaturization and enhanced functionality.

In the past several years, significant research efforts have been reported that strongly substantiate the promise of graphene for THz optoelectronics. The present article is focused on work in this area involving the use of graphene plasmonic oscillations. The fundamental physics of these excitations and their initial experimental observation are reviewed in Section 2. In particular, the active tunability of the plasmonic resonance frequency is discussed in detail for two representative configurations, graphene nanoribbons and grating-coupled graphene films. The key factors determining the plasmonic absorption strength, including doping and the interplay between radiative and nonradiative damping, are also described together with possible avenues to maximize the underlying light–matter interactions. Various THz device applications from the recent literature are then presented in Sections 3 and 4. The use of plasmonic effects in graphene is particularly significant as a way to increase the fraction of incident light that can be absorbed, which in 2D materials is intrinsically limited by their ultrasmall thickness. This general idea has been employed successfully in several demonstrations of THz modulators and photodetectors, and representative results for both types of devices are reviewed in Section 3. Next, Section 4 describes initial work towards the development of graphene THz light sources, including devices based on plasmon amplification in the presence of population inversion and plasmonic emitters where GPPs are excited by an injected electrical current (through the generation and subsequent energy relaxation of hot carriers) and then radiate into the far field. A theoretical model for the latter radiation mechanism is also presented that highlights the importance of plasmon-enhanced light–matter interactions for this application as well. The current status and potential of all these device technologies are finally summarized in the conclusive Section 5.

2 Graphene plasmon polaritons

Surface plasmon polaritons are guided electromagnetic waves propagating along the interface between a conductor and an insulator, coupled to collective oscillations of the electron gas at the surface of the conductor. By virtue of their highly evanescent nature, they can feature deeply sub-wavelength optical confinement with strong local field enhancement, at the expense however of substantial optical losses due to ohmic absorption in the conductor. These properties have been widely investigated in the past couple of decades for applications such as surface-enhanced sensing and spectroscopy, imaging beyond the diffraction limit, medical diagnostics and treatment, high-efficiency photovoltaics, etc. [30]. Typical plasmonic devices consist of films or nanostructures of noble metals (Au, Ag, Al) with resonant excitations at near-infrared or visible wavelengths. Since the plasma frequency of a conductor generally increases with its carrier density, longer-wavelength plasmonic excitations (extending into the THz spectral region) can be obtained with doped semiconductors, either at the free surface of bulk films [31] or in the two-dimensional electron gas (2DEG) of buried heterojunctions [32]. As a 2D semimetal with widely gate-tunable carrier density, graphene is also particularly interesting for basic studies and device applications in plasmonics. While several review articles already exist [10, 24–27], here we discuss the fundamental properties of GPPs that are directly relevant to the THz devices described in the following. It should also be noted that GPPs are only one example of a rich family of tunable polaritonic excitations in 2D materials and van der Waals heterostructures [33].

2.1 Plasmonic dispersion properties

We begin by considering a planar sheet of graphene surrounded by two dielectric media of relative permittivities ε_{r1} and ε_{r2} [Figure 1]. This system supports a continuous distribution of plasmon polariton modes, whose dispersion properties can be computed by solving Maxwell's equations in the space immediately below and above the sheet and then applying the electromagnetic boundary conditions. In this formulation, graphene is described by means of its conductivity function $\sigma(\omega, \beta)$, where ω is the optical angular frequency and β is the wavenumber. If we consider the nonretarded regime ($\beta >> \omega/c$) and use a simple Drude model for σ, the following dispersion relation is obtained [34, 35]:

$$\beta(\omega) = \frac{\pi\hbar^2\epsilon_0(\varepsilon_{r1}+\varepsilon_{r2})}{q^2 \mathrm{E_F}}\left(1+\frac{i}{\omega\tau}\right)\omega^2, \qquad (1)$$

where τ is the relaxation time accounting for all relevant electronic scattering mechanisms and E_F is the Fermi energy. Despite the simplicity of the Drude model, this expression can be quite accurate provided that two key conditions are satisfied [35]. First, the graphene Fermi level E_F must be sufficiently larger than the thermal energy $k_B T$ so that finite-temperature effects can be neglected. Second, the frequency ω must be small enough so that interband damping (where GPPs are absorbed through the excitation of electron-hole pairs) is forbidden by Pauli blocking. When the latter condition is not satisfied, a more accurate model can be constructed using the random phase approximation for the dynamic conductivity, including the contribution from interband transitions [34]. In any case, for the typical carrier densities (of order 10^{12} cm^{-2}) and frequencies (<10 THz) considered in this review, the Drude model underlying Eq. (1) has been shown to be fully appropriate [36]. It is also interesting to note that the characteristic features of Eq. (1), including the ω^2 and $1/E_F$ dependence of the real part of β, are a general property of plasmon polaritons in any 2DEG [37]. The dependence on carrier density per unit area N, however, is determined by the electronic band structure. In graphene, due to the conical dispersion near the Dirac points, $\mathrm{E_F} = \hbar \mathrm{v_F}\sqrt{\pi \mathrm{N}}$ (where $\mathrm{v_F} \approx 1 \times 10^8$ cm/s is the Fermi velocity) so that $\beta \propto 1/\sqrt{\mathrm{N}}$. In contrast, in traditional semiconductor 2DEGs with a parabolic energy dispersion, $\beta \propto 1/\mathrm{N}$.

The propagation constant Re[$\beta(\omega)$] of Eq. (1) can be substantially larger than the free-space wavenumber $k_O = \omega/c$ at the same frequency, by one to two orders of magnitude depending on the specific values of all the relevant parameters. As a result, the wavelength and transverse localization length of GPPs can be smaller than the free-space wavelength by the same factor, leading to extreme optical confinement. At the same time, according to Eq. (1) the ratio between the real and imaginary parts of $\beta(\omega)$, which determines the quality factor of the plasmonic oscillations, is equal to $\omega\tau$. While this result is again common to all 2DEGs, it should be noted that the relaxation time τ in graphene can be particularly long, even at room temperature where the electronic mobility of traditional

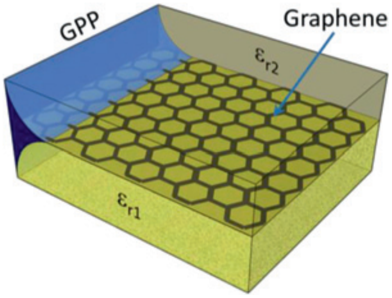

Figure 1: Graphene plasmon polaritons. Schematic illustration of the GPP field-intensity distribution (shown in blue) for a continuous sheet of graphene embedded within two homogeneous dielectric media of permittivity ε_{r1} and ε_{r2}.

semiconductors is significantly degraded by phonon scattering. In graphene, by virtue of its large optical phonon energies and weak electron-phonon coupling, the mobility (proportional to τ) is instead often limited by scattering mechanisms originating from the substrate, such as charged impurities and surface roughness. As a result, record large room-temperature mobilities can be achieved in samples embedded within highly inert hexagonal-BN (h-BN) layers [18, 19] or partially suspended [16, 17]. The same geometries can therefore be employed to produce plasmon polaritons with particularly low propagation losses and high quality factors, as confirmed by recent experimental studies [38, 39]. More in general, graphene offers a more favorable tradeoff between optical losses and field confinement compared to other plasmonic systems including noble-metal nanostructures.

Equation (1) also indicates that the dispersion properties of GPPs depend on the surrounding materials through their permittivities $\varepsilon_{\mathrm{r1}}$ and $\varepsilon_{\mathrm{r2}}$. A particularly common substrate for fundamental studies and device applications of graphene is oxidized silicon in a gated field-effect-transistor (FET) configuration. In this arrangement, the medium above the graphene sheet is air (i. e., $\varepsilon_{\mathrm{r2}} = 1$), while the medium below consists of an $\mathrm{SiO_2}$ layer of sub-micron thickness t_{OX} on a doped Si substrate. If the Si crystal has sufficiently low doping to behave as a (lossy) dielectric at the plasmonic frequencies of interest, Eq. (1) remains approximately valid with the permittivity ε_{r1} given by a weighted average of those of $\mathrm{SiO_2}$ and Si. The relative weights are determined by the overlap factors of the plasmonic field-intensity distribution [which varies with distance z from the graphene plane approximately as $\exp(-2\mathrm{Re}[\beta(\omega)]|z|)$] with the two materials. In contrast, if the Si doping is large enough to produce a negative permittivity at the GPP frequencies, the plasmonic dispersion properties are significantly modified by the additional metallic boundary condition at the Si/$\mathrm{SiO_2}$ interface. Under these conditions, for sufficiently small t_{OX} a linear relation between wavenumber β and angular frequency ω is obtained [40], similar to the behavior of acoustic waves.

Regardless of the details of the surrounding media, GPPs in continuous films cannot be excited directly by incident radiation, whose in-plane wavevector is always smaller than the free-space wavenumber k_O, which in turn is much smaller than the plasmonic propagation constant $\mathrm{Re}[\beta]$. This limiting behavior is again common to surface plasmon polaritons in other 2DEGs or at planar metal-dielectric interfaces, and several different approaches have been devised to overcome it. For the direct study of GPP propagation, near-field microscopy techniques have been employed to excite and monitor these surface waves [38, 41–44], by taking advantage of the highly evanescent optical fields that can be produced and collected by nanotips. Specifically, these measurements allow visualizing the standing-wave patterns generated by the reflection of GPPs at the edges of graphene films and nanostructures, as well as at internal line defects such as grain boundaries [43]. To enable direct coupling to free-space radiation, as needed in typical device applications, subwavelength graphene structures such as nanoribbons [45–49] or disks [50–52] have been used as a way to effectively eliminate the requirement of in-plane momentum conservation. Alternatively, the momentum mismatch between free-space radiation and GPPs in continuous films can be compensated by diffractive coupling with a periodic array. The latter approach has been demonstrated using graphene sheets near a surface relief grating [53–55], coated with a periodic array of nanoparticles [56], or patterned in the shape of a periodic lattice of holes (anti-dots) [52, 57, 58].

2.2 Plasmonic resonances of graphene nanoribbons

For any given coupling geometry, the GPP resonance frequencies can be tuned by design through the structure dimensions and actively by varying the graphene carrier density. As a first important example, in Figure 2(a) we consider an array of graphene nanoribbons of width w, connected between the source and drain contacts in a gated FET configuration. In this geometry, each nanoribbon acts as a Fabry–Perot cavity for plasma waves along the direction perpendicular to its long axis [the x direction of Figure 2(a)]. The plasmonic resonance frequencies ω_n are then determined by the phase condition requiring constructive interference upon each roundtrip within the cavity, i. e., $2\mathrm{Re}[\beta(\omega_n)]w + 2\varphi_r = 2n\pi$, where φ_r is the reflection phase for plasma waves at each ribbon edge and n is a positive integer. The reflection phase can take on nontrivial values due to the presence of strong evanescent fields at the graphene edges, and a value of (or near) $\pi/4$ has been computed [59, 60]. Using Eq. (1) for the GPP wavenumber $\beta(\omega)$ and the aforementioned relation between Fermi energy E_F and carrier density N, the following simple analytical expression is obtained for the resonance frequencies $\nu_n = \omega_n/(2\pi)$:

$$\nu_n = \frac{1}{2\pi}\sqrt{\frac{q^2 \mathrm{v_F}\left(n\pi - \phi_r\right)}{\sqrt{\pi}\hbar\varepsilon_0\left(\varepsilon_{r1} + \varepsilon_{r2}\right)}}\,\frac{\mathrm{N}^{1/4}}{\sqrt{w}}. \tag{2}$$

More specifically, this equation describes the nanoribbon plasmonic modes with zero longitudinal wavenumber. For each value of the integral index *n*, a continuous distribution of GPPs also exist that propagate along the nanoribbon in the *y* direction, while bouncing back and forth between its boundaries along the *x* direction according to the phase condition above. Importantly, however, the resulting plasmonic density of modes is peaked at the resonance frequencies of Eq. (2) [61], so that the nanoribbon optical response is typically dominated by the GPPs at these frequencies. In arrays of nanoribbons, the plasmonic resonance frequencies can also be affected by near-field coupling between neighboring ribbons at sufficiently small separations (~10 nm) [61].

In Figure 2(b) we plot the frequency of the fundamental plasmonic resonance ν_1 computed as a function of carrier density *N*, for different values of the nanoribbon width *w* in the FET geometry of Figure 2(a). This oxidized-Si FET geometry is particularly convenient and well established for the purpose of tuning the graphene carrier density *N* dynamically with an electrical signal. Specifically, *N* is determined by the capacitor relation $q\text{N} = \varepsilon_0\varepsilon_{\text{OX}}|\text{V}_\text{G} - \text{V}_\text{CNP}|/t_{\text{OX}}$, where ε_{OX} and t_{OX} are the permittivity and thickness of the SiO_2 gate dielectric, respectively, V_G is the applied voltage between the back gate and the graphene channel, and V_CNP is the gate voltage at charge neutrality. For typical values of t_{OX} on the order a few 100 nm, the carrier-density values considered in Figure 2(b) can be achieved with practical gate voltages on the order of several 10 V. Therefore, it follows from this plot that the fundamental plasmonic resonance of graphene nanoribbons can be tuned, actively and by design, across the entire THz spectrum. In fact, mid-infrared resonances can also be produced with the same configuration using narrower ribbons [46, 47].

This nanoribbon geometry was employed in the first experimental observation of GPPs excited by free-space radiation [45]. The devices used in these measurements are based on graphene grown by chemical vapor deposition (CVD) on copper and then transferred on an oxidized Si substrate with a poly(methyl methacrylate) (PMMA) support polymer. The ribbon arrays, shown in the atomic force microscopy (AFM) images of Figure 2(c), were fabricated by photolithography and oxygen plasma etching. A thin ion-gel top-gate architecture was also introduced in order to control the graphene carrier density over a particularly large range, up to 15 × 10^{12} cm^{-2}, with small voltages on the order of a few V. Optical transmission spectra measured with these devices at room temperature [Figure 2(d) and (e)] reveal strong absorption features in the spectral range between 100 and 200 cm^{-1} (3–6 THz), with peak value as large as 13%. The expected tunability with ribbon width [Figure 2(d)] and carrier density [Figure 2(e)] is also clearly demonstrated by these data. Additionally, Figure 2(e) shows that plasmonic absorption in these devices is only experienced by light polarized perpendicular to the nanoribbons. In contrast, a monotonic increase in absorption with decreasing frequency is observed with the opposite polarization (as shown in the figure inset), indicative of free-

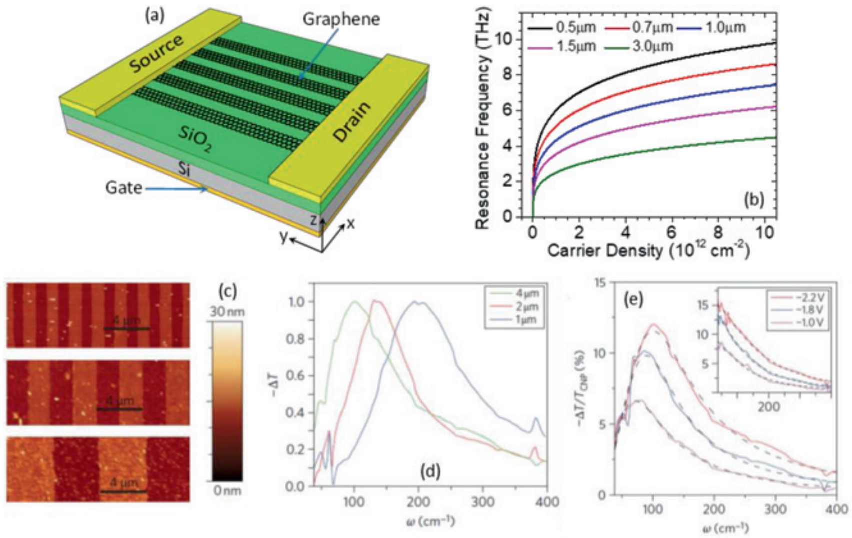

Figure 2: Graphene nanoribbons. (a) Schematic illustration of a graphene nanoribbon device in a gated FET configuration. (b) Resonance frequency of the fundamental plasmonic resonance of the same device structure, calculated as a function of carrier density N for different values of the nanoribbon width w. (c) AFM images of three devices with w = 1, 2, and 4 µm. (d) Normalized absorption spectra of the devices of (c) at a carrier density N of 15 × 10^{12} cm^{-2}, for incident light polarized perpendicular to the nanoribbons. (e) Absorption spectra of the 4 µm-width sample for different values of the gate voltage $\text{V}_{\text{GS}} - \text{V}_{\text{CNP}}$ (applied across a top gate dielectric). The inset shows the spectra measured under the same conditions with incident light polarized parallel to the nanoribbons. In (d) and (e), ΔT indicates the difference between the sample transmission coefficient T at a given gate voltage and its value at charge neutrality T_{CNP}. (c)–(e): reprinted with permission from ref. [45]. Copyright (2011), Springer Nature.

carrier absorption. This behavior is consistent with the polarization properties of surface plasmon polaritons, which generally possess an in-plane component of the electric field parallel to their direction of propagation [30]. As discussed above, the dominant plasmonic excitations of graphene nanoribbons propagate back and forth between the ribbon edges at normal incidence. Therefore, these oscillations cannot be excited by incident light polarized parallel to the nanoribbons.

2.3 Plasmonic resonances of grating-coupled graphene

An alternative approach for the coupling of GPPs to free-space radiation involves the use of a diffraction grating located in the near-field vicinity of the graphene active layer. A possible device geometry for this purpose is shown schematically in Figure 3(a) [56], where the grating consists of a square-periodic array of gold nanocylinders deposited on a continuous sheet of graphene. A potential advantage of this geometry is a particularly simple fabrication process, where the array is introduced in the same lithography steps as the metal contacts. Therefore, compared to graphene nanostructures such as the nanoribbons of the previous section, this approach does not require any complex shaping of the graphene sheet, where irregular and defective edges may be introduced. Compared to other grating-coupled configurations [53–55], it does not require the transfer of graphene on a patterned substrate, where inhomogeneous strain fields may be produced leading to the formation of crystalline defects. As a result, for any given graphene synthesis and deposition process, particularly high structural quality of the GPP active layer can be expected.

In general, diffractive coupling relies on the ability of a grating of period Λ along the x (y) direction to shift the x (y) component of the incident-light wavevector by any integral multiple of $2\pi/\Lambda$. In the square-periodic array of Figure 3(a), a GPP of angular frequency $\omega_{n.m}$ can therefore be excited if its propagation constant matches the shifted in-plane wavevector, i. e., $\mathrm{Re}[\beta(\omega_{n,m})] = 2\pi\sqrt{n^2+m^2}/\Lambda$, where n and m are two integers specifying the diffraction order. It should be noted that this equation neglects the in-plane wavevector of the incident light, which is generally much smaller than $\mathrm{Re}[\beta]$ as mentioned previously. Using Eq. (1), the following expression is then obtained for the grating-coupled GPP resonance frequencies $\nu_{n,m} = \omega_{n,m}/(2\pi)$ (i. e., the frequencies of the excited GPPs),

$$\nu_{n,m} = \frac{1}{2\pi}\sqrt{\frac{2\sqrt{\pi}q^2 \mathrm{v}_F\sqrt{n^2+m^2}}{\hbar\epsilon_0(\varepsilon_{r1}+\varepsilon_{r2})}}\,\frac{\mathrm{N}^{1/4}}{\sqrt{\Lambda}}. \tag{3}$$

These frequencies exhibit a similar dependence on carrier density and structural dimensions as the nanoribbon resonances of Eq. (2), and can also span a wide portion of the THz spectrum [Figure 3(b)]. It should also be noted that the fundamental diffraction resonances ($n = 1$, $m = 0$) and ($n = 0$, $m = 1$) can only be excited by incident light polarized along the x and y directions, respectively, because of the aforementioned polarization properties of surface plasmons [30]. However, in the

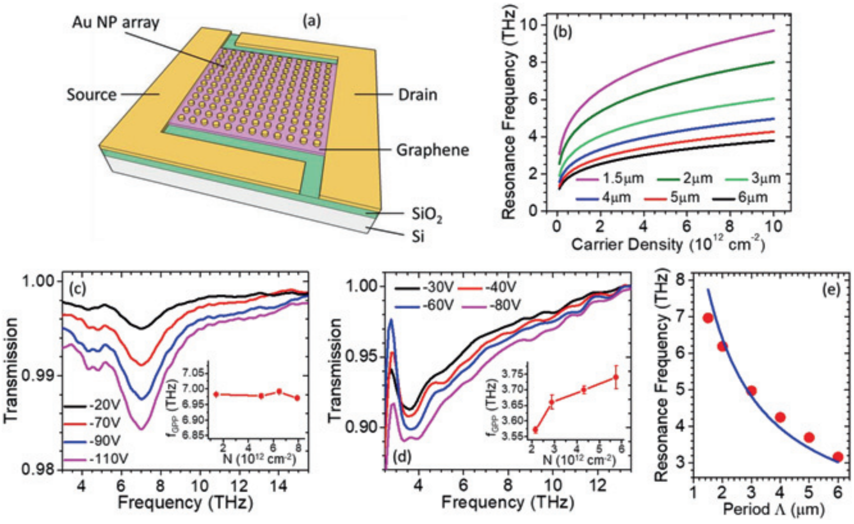

Figure 3: Grating-coupled graphene. (a) Schematic illustration of a graphene FET coated with a periodic array of Au nanoparticles (NPs). (b) Frequency of the first-order plasmonic resonance of the same device structure, calculated as a function of carrier density N for different values of the array period Λ. (c), (d) Transmission spectra of two devices with array period $\Lambda = 1.5$ μm (c) and 5 μm (d) for different values of the gate voltage V_{GS}, normalized to the spectra at the charge neutrality point. Inset: frequency of minimum transmission f_{GPP} as a function of carrier density N (estimated from V_{GS} using the gate capacitor relation with $t_{OX} = 300$ nm). (e) Symbols: measured values of f_{GPP} versus Λ for six different samples. Solid line: theoretical fit of the experimental data based on the expression of Eq. (3) for $f_{GPP} = \nu_{1,0} = \nu_{0,1}$, with N used as the only fitting parameter; a fairly good agreement is obtained for $N = 4.1 \times 10^{12}$ cm^{-2}. Reprinted with permission from ref. [56]. Copyright (2017), American Chemical Society.

square-periodic array under study, these two modes are degenerate so that their superposition is polarization independent.

Representative experimental results obtained with this grating-coupled device geometry are shown in Figure 3(c)–(e) [56], for a set of samples based on large-area (~1 mm^2) graphene sheets grown by CVD on copper and transferred on oxidized Si substrates using PMMA. In order to enable gated transmission measurements, the FET gate contact in these devices is deposited on a small window etched through the top SiO_2 layer (as opposed to the back surface of the Si substrate). With this approach, pronounced THz absorption dips were measured at room temperature [Figure 3(c) and (d)], with center frequencies varying with grating period Λ in good agreement with Eq. (3) [Figure 3(e)]. Particularly large quality factors (for CVD graphene) of up to about four are also observed in some of these plots. At the same time, as the gate voltage V_{GS} is increased, the amplitudes of these transmission dips increase but their center frequencies remain relatively constant [see insets of Figure 3(c) and (d)], in apparent discrepancy with the theoretical predictions plotted in Figure 3(b). This unexpected behavior is attributed to large variations in carrier density N across the sample area for fixed V_{GS}, which were also measured with the same samples by Raman microscopy [56] consistent with prior reports [62]. As a result, the plasmonic absorption spectra appear to be dominated by the sample regions with carrier density values in the range corresponding to maximum scattering lifetime (~2–5 × 10^{12} cm^{-2} for graphene on SiO_2 [63]), where the diffractive coupling of incident light to GPPs can be expected to be strongest as discussed in the next section. This observation provides important insight on the limits of tunability of GPPs, especially in large-area samples, and highlights the importance of uniform carrier distribution to enable dynamically tunable graphene plasmonic devices.

2.4 Plasmonic absorption and critical coupling

From an application standpoint, GPPs are attractive as a means to enhance the strength of light–matter interactions in graphene (absorption, emission, nonlinear frequency conversion), which is otherwise necessarily limited by the single-atomic-layer thickness of the graphene lattice. To illustrate their potential and limitations for this purpose, here we discuss how GPPs contribute to the absorption strength of the gated nanoribbons of Figure 2. The key conclusions of this discussion can then be extended to other device geometries and optical processes. In general, the plasmonic absorption spectrum $\alpha_{GPP}(\nu)$ can be computed via finite-difference time-domain (FDTD) simulations by comparing incident, reflected, and transmitted power for a single unit cell of the device structure under study. Figure 4(a) shows the calculated spectra of a representative device (having 530 nm nanoribbon width and 1 μm center-to-center spacing), for light at normal incidence with polarization perpendicular and parallel to the nanoribbons. The carrier mobility μ used in these simulations [proportional to

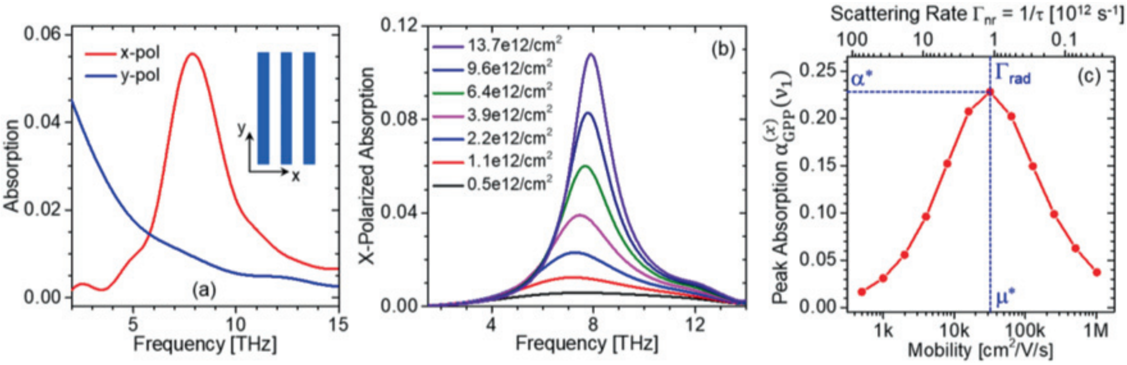

Figure 4: Plasmonic absorption in graphene nanoribbons. (a) Absorption spectrum for incident light with polarization parallel (blue trace) and perpendicular (red trace) to the nanoribbons, for $\mu = 2{,}000$ cm^2/Vs and $N = 5.4 \times 10^{12}$ cm^{-2}. The nanoribbons have 530 nm width and 1000 nm center-to-center spacing. (b) X-polarized absorption spectra for different nanoribbons at different carrier densities. The ribbon widths, selected to produce approximately the same peak absorption frequency, vary from 200 to 800 nm in steps of 100 nm in order of increasing carrier density. In each sample, the mobility is $\mu = 2{,}000$ cm^2/Vs and the geometrical fill factor is 50%. (c) Peak absorption of the structure of (a) for x-polarized light versus mobility (bottom axis) and plasmonic nonradiative damping rate (top axis). For simplicity, the SiO_2 gate dielectric is modeled with a real dielectric constant in these simulations, so that the calculated absorption values are due entirely to the graphene nanoribbons.

the scattering lifetime τ of Eq. (1)] is 2,000 cm^2/Vs, which is appropriate for CVD graphene deposited on SiO_2 using PMMA [64]. The Fermi energy E_F is 0.27 eV (corresponding to a carrier density of 5.4×10^{12} cm^{-2} for $t_{OX} = 300$ nm), large enough so that interband absorption at THz frequencies is completely suppressed due to Pauli blocking.

The results plotted in Figure 4(a) are consistent with the polarization properties described in Section 2.2, i. e., nanoribbon GPPs can only be excited by light polarized perpendicular to the ribbons. At the same time, even with the proper incident polarization, the absorption strength at the plasmonic resonance frequency (i. e., the fraction of incident light absorbed by the GPPs) is found to be relatively small, less than 6%. A particularly simple approach to increase this peak absorption is to use wider nanoribbons with higher carrier density, where the size mismatch between the plasmonic field distribution and the incident wavelength is reduced while more electrons (or holes) can contribute to the plasmonic oscillator strength. This idea is illustrated in Figure 4(b), where we plot the x-polarized absorption spectra of several structures with different combinations of ribbon width w and carrier density N, each selected to produce approximately the same resonance frequency ν_1 following Eq. (2). In practice, this approach is ultimately limited by the maximum available gate voltage and/or dielectric breakdown in the gate insulator, as well as by the decrease in mobility at exceedingly large carrier densities. A related approach involves the use of samples consisting of two (or more) graphene sheets stacked on top of one another. Recent work has established that the effective Fermi energy E_F for plasmonic oscillations in double-layer graphene (DLG) is equal to the sum of the Fermi levels of the individual layers [65]. As a result, given the nonlinear relation between carrier density and Fermi energy in graphene ($N \propto E_F^2$), DLG allows accessing the same plasmonic frequencies with larger nanoribbon dimensions, which again is favorable to increase the absorption strength.

To further elucidate the key limiting factors of graphene plasmonic absorption, in Figure 4(c) we plot the calculated x-polarized peak absorption $\alpha_{GPP}^{(x)}(\nu_1)$ of the same device of Figure 4(a) at the same carrier density as a function of carrier mobility μ (bottom axis) and corresponding scattering rate $1/\tau$ (top axis). The shape of this trace can be explained with a general argument based on coupled-mode theory [66, 67]: the coupling between external radiation and the plasmonic resonance is maximum when the radiative decay rate of the plasmonic oscillations Γ_{rad} is equal to their nonradiative damping rate Γ_{nr}. Away from this critical-coupling condition, the absorption decreases regardless of whether $\Gamma_{rad} < \Gamma_{nr}$ (under-coupling) or $\Gamma_{rad} > \Gamma_{nr}$ (over-coupling). In the graphene 2DEG, nonradiative damping of the plasmonic oscillations involves the same scattering mechanisms that also limit the mobility (impurities, defects, phonons, and other carriers). Therefore, Γ_{nr} can be taken to be equal to $1/\tau$, which is inversely proportional to μ. The radiative decay rate Γ_{rad} is instead largely independent of electronic scattering processes and mostly limited by the large wavelength mismatch between the graphene surface plasmons and free-space radiation. The simulation results of Figure 4(c) indicate that, in the nanoribbon geometry under study, critical coupling is achieved at an optimal mobility $\mu^\star$ of about 30,000 cm^2/Vs. Therefore, samples based on CVD graphene on oxidized Si [with typical mobilities on the order of 2,000 cm^2/Vs, as in Figure 4(a) and (b)] are strongly under-coupled. Additionally, Figure 4(c) also shows that the peak absorption of the same device under critical coupling, $\alpha^\star = 23\%$, is well below its theoretical limit of 100%.

These considerations suggest several possible avenues to further improve the design of graphene plasmonic nanostructures for enhanced light–matter interactions. First, higher-quality graphene samples with larger mobility may be employed. In fact, mobilities approaching the optimal value for critical coupling in Figure 4(c) can be achieved, even at room temperature, with graphene sheets embedded in h-BN [18, 19] or partially suspended [16, 17]. However, at present these samples tend to be quite small and cannot be readily scaled to the lateral dimensions required to avoid diffraction-limit effects in THz optoelectronic devices (≳100 μm). Second, the graphene nanostructures may be combined with additional photonic and/or plasmonic antennas that can effectively “funnel” incident radiation into the GPPs (and vice versa) [68, 69], in order to increase their radiative decay rate Γ_{rad} and thus lower the optimal mobility $\mu^\star$. Finally, the graphene dielectric environment may also be engineered to increase the peak plasmonic absorption at critical coupling [$\alpha^\star$ in Figure 4(c)] towards its maximum possible value of 100%. In general, $\alpha^\star$ in these devices is limited by the presence of both transmission and reflection channels for the incident light, in addition to absorption, and therefore perfect absorption may be achieved by suppressing these additional processes [70, 71]. Specific configurations that have been developed to increase Γ_{rad} and/or $\alpha^\star$ will be discussed in the next chapter, in the context of graphene THz modulators.

3 Graphene THz devices based on plasmonic absorption

The fundamental physical properties of graphene plasmonic excitations, and the ability to control them by design in nanostructures of increasing complexity, remain the subject of extensive ongoing research. At the same time, in the past several years, considerable efforts have also been devoted to the exploration of their optoelectronic device applications at both THz and mid-infrared wavelengths. These activities so far have primarily focused on optical modulators and photodetectors, and in the following we describe some of the main accomplishments and opportunities for further progress in the context of THz optoelectronics. Related work, also with significant device implications, includes the use of GPPs for THz difference frequency generation [72, 73] and mid-infrared biosensing [74, 75]. Additionally, it should be noted that an extensive literature also already exists on the demonstration of various types of graphene THz modulators [76–82] and photodetectors [83–85] that do not involve GPPs.

3.1. THz optical modulators

The broadband dynamic tunability and relatively narrow linewidth of plasmonic absorption in graphene are particularly well suited for the development of optical modulators. In such devices, the fraction of incident light transmitted through the graphene active material is modulated by varying the applied gate voltage. In the off-state, transmission is minimized by tuning the plasmonic resonance under high carrier density to the desired operation wavelength. The on-state is then produced by varying the gate voltage to decrease the carrier density, so as to simultaneously suppress and red-shift the plasmonic absorption peak. This basic device functionality is illustrated by the absorption spectra of Figure 2(e) [45]. In this particular example, a modulation efficiency (i. e., fractional decrease in transmission from the on- to the off-state) of about 10% is obtained at frequencies near 100 cm^{-1} (3 THz) for a change in gate voltage (across a thin ion-gel top-gate dielectric) on the order of 1 V. The corresponding modulation speed is limited by the RC time constant associated with the gate capacitor and its series resistance, and GHz-range cutoff frequencies are expected to be accessible with an optimized design of the gating configuration [68].

The key challenge for the development of practical devices based on this principle is provided by the relatively small single-pass absorption of graphene (even at the GPP resonance frequency), which limits the maximum achievable modulation depth. For some applications, the graphene active layer could be integrated with a waveguide configuration, e. g., for the direct current modulation of the radiation output of a THz QCL [86]. More generally, a possible solution is the introduction of additional THz antennas that can focus the incident light into sufficiently small “hot spots” overlapping the graphene plasmonic oscillators. As a result, the GPP radiative decay rate Γ_{rad} can be enhanced, as discussed in the previous section, leading to increased absorption. This approach has been employed in ref. [68], where graphene nanoribbons were integrated within the capacitor gaps of an array of complementary split-ring resonators (C-SRRs) patterned in a metal film [Figure 5(a)]. These structures can be described as lumped LC circuit elements at optical frequencies, featuring a geometrically tunable transmission resonance [dashed curve in Figure 5(b)]. The graphene nanoribbons (fabricated from CVD-grown graphene transferred on a Si/SiO$_2$ substrate) introduce an additional absorption resonance, which can be tuned dynamically by varying the gate voltage as described in Section 2.2. When the two resonances overlap, the transmission at their common center frequency is minimized. In Figure 5(b), an on/off modulation efficiency of about 60% near 4 THz is demonstrated based on this approach. The corresponding change in gate voltage in this device is quite large (about 100 V), but could be reduced substantially using a thinner gate dielectric, such as the ion gel used in ref. [45]. The structure of Figure 5 was also found to display the hallmarks of strong coupling between the underlying resonances [68], and therefore provides an interesting platform for studying cavity-enhanced light–matter interactions at THz frequencies.

Further improvements in modulation depth could be achieved with device structures that can provide perfect absorption under conditions of critical coupling. A possible design is shown in Figure 6(a), where a back Au mirror is used to block transmission of the incident light and at the same time suppress reflection through interference (with the proper choice of graphene-mirror separation). As a result, perfect absorption is enforced by the requirement of conservation of power flow [70, 71]. This basic structure is well established in radio-wave engineering [87], where it is referred to as Salisbury screen. To illustrate its effectiveness, in Figure 6(b) we plot the calculated peak absorption $\alpha_{\text{GPP}}^{(x)}(\nu_1)$ of an array of graphene nanoribbons on an optimized vertical cavity as a function of graphene mobility μ. The nanoribbon width (w = 530 nm) and carrier density (N = 6.5×10^{12} cm^{-2}) are similar to those of the device of Figure 4(c), resulting in the same resonance frequency (7.9 THz). A maximum

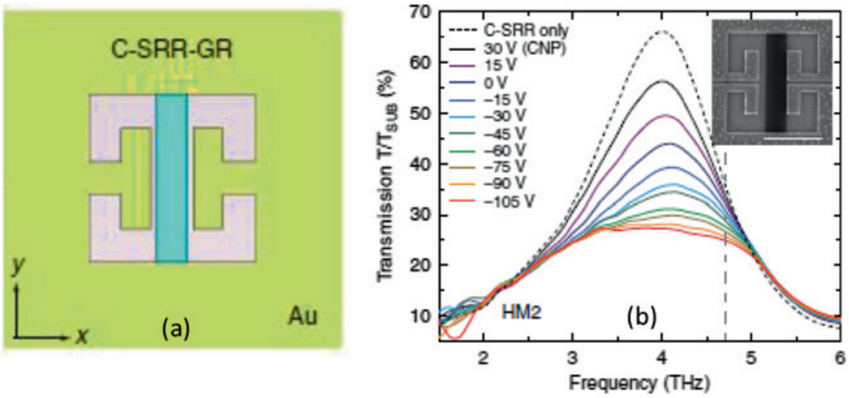

Figure 5: Hybrid graphene metamaterial for THz modulation. (a) Schematic illustration of a unit cell, consisting of a graphene nanoribbon (light blue rectangle) located in the capacitor gap of a complementary split-ring resonator patterned in a Au film. (b) Transmission spectra of a device consisting of an array of closely packed unit cells based on the design of (a) at different back-gate voltages. Each spectrum is normalized to the substrate transmission. The dashed curve was measured with a reference device without the graphene nanoribbons. Inset: SEM image of a unit cell (the scale bar is 5 μm). Reprinted with permission from ref. [68]. Copyright (2015), Springer Nature.

graphene absorption of over 99% is obtained with this device at the optimal mobility for critical coupling $\mu^\star$ (again ~30,000 cm^2/Vs), and at any mobility its peak absorption is larger than that of the reference structure of Figure 4(c) by a factor of over 4. Additionally, even though the device operation mechanism relies on interference, active tunability can still be achieved. This conclusion is substantiated in Figure 6(c), where we plot the absorption spectrum $\alpha_{\mathrm{GPP}}^{(x)}(\nu)$ of the same structure of Figure 6(b) at $\mu = 32{,}000$ cm^2/Vs for different values of the Fermi energy. Theoretical considerations also indicate that this perfect absorption mechanism is nearly omnidirectional [70].

Finally, even in this Salisbury-screen configuration the optimal mobility $\mu^\star$ can be decreased towards values accessible with CVD graphene by combining the graphene plasmonic oscillators with suitable antennas that can enhance the GPP radiative decay rate Γ_{rad}. This idea has been demonstrated in recent work at mid-infrared wavelengths (near 7 μm) [69], where simple Au rectangular antennas were introduced in an array of CVD-graphene nanoribbons with mobility smaller than 1000 cm^2/Vs. Both graphene and Au nanostructures were fabricated on a SiO_2/SiN_x membrane of the required thickness to suppress reflection (approximately one quarter of the target wavelength rescaled by the membrane refractive index), back coated with a Au film. With this device, a maximum absorption of nearly 97% was measured, together with an on/off modulation efficiency of about 96% in reflection. The same approach could be extended to THz modulators by rescaling both the antenna dimensions and the cavity thickness.

3.2. THz photodetectors

The use of graphene for photodetection across the entire infrared spectrum has also been investigated extensively over the past decade [88]. Similar to the modulator application just described, a key requirement to improve the performance of graphene photodetectors is to increase the fraction of incident light that can be absorbed in the active layer to produce a readout electrical signal. Once again, plasmonic effects are attractive for this purpose, although it is important to point out that plasmonic absorption is an intrinsically intraband process, where optical energy is transferred to the electron (or hole) gas without the direct creation of additional electron-hole pairs. As a result,

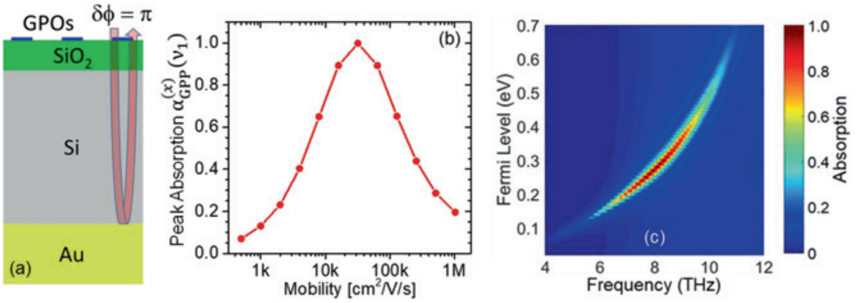

Figure 6: Graphene plasmonic oscillators (GPOs) on a vertical cavity for THz modulation. (a) Schematic device geometry. (b) Calculated peak absorption versus mobility, for an array of graphene nanoribbons (with 530 nm width, 4.4 μm center-to-center spacing, and 6.5×10^{12} cm^{-2} carrier density) on an optimized vertical cavity (with 2.7 μm Si thickness and 300 nm SiO_2 thickness). (c) Absorption of the same device versus frequency and Fermi energy for μ = 32,000 cm^2/Vs. In all these simulations, the device is illuminated at normal incidence with light polarized perpendicular to the nanoribbons.

standard photoconductive and photovoltaic devices (which rely on the photoexcitation of electrons and holes and their subsequent separation under an external or built-in voltage) would not benefit from plasmonic enhancement effects. However, additional photodetection mechanisms have also been reported in graphene that involve a photoinduced increase in carrier temperature rather than density, including the bolometric and photo-thermoelectric effects [88]. In a bolometer, this temperature increase is detected through the corresponding change in conductivity, due to either a decrease in mobility or an increase in carrier density after thermal equilibration [89]. In a photo-thermoelectric device, a photocurrent is produced through the Seebeck effect in suitably asymmetric device structures (e. g., employing different metals in the source and drain electrodes) [84]. These photodetection mechanisms are actually especially important in graphene by virtue of its weak electron-phonon coupling, so that the electron gas can reach significantly higher temperatures than the lattice. Furthermore, they can generally be expected to play a dominant role in devices operating at long infrared wavelengths (especially THz) where interband transitions are suppressed by Pauli blocking.

In this context, plasmonic absorption can again be quite beneficial. Similar to what happens in other plasmonic systems [90], optically excited GPPs predominantly decay into hot carriers, which then rapidly thermalize with one another (on a typical time scale of a few ten femtoseconds) at an elevated temperature over the lattice. In fact, because of the comparatively small number of electrons involved in the plasmonic oscillations in graphene, a particularly large temperature increase can be expected for any given amount of absorbed optical energy [25]. As a result, the responsivity of any photodetector relying on carrier heating can be enhanced by incorporating plasmonic structures to increase the optical absorption. This idea was initially demonstrated at mid-infrared wavelengths (near 10 μm) in ref. [91], with an array of CVD-graphene nanoribbons in an FET configuration [Figure 7(a)]. When the gate voltage is tuned so that the GPP resonance matches the incident wavelength, a large increase in photocurrent (up to 15-fold) is obtained for light

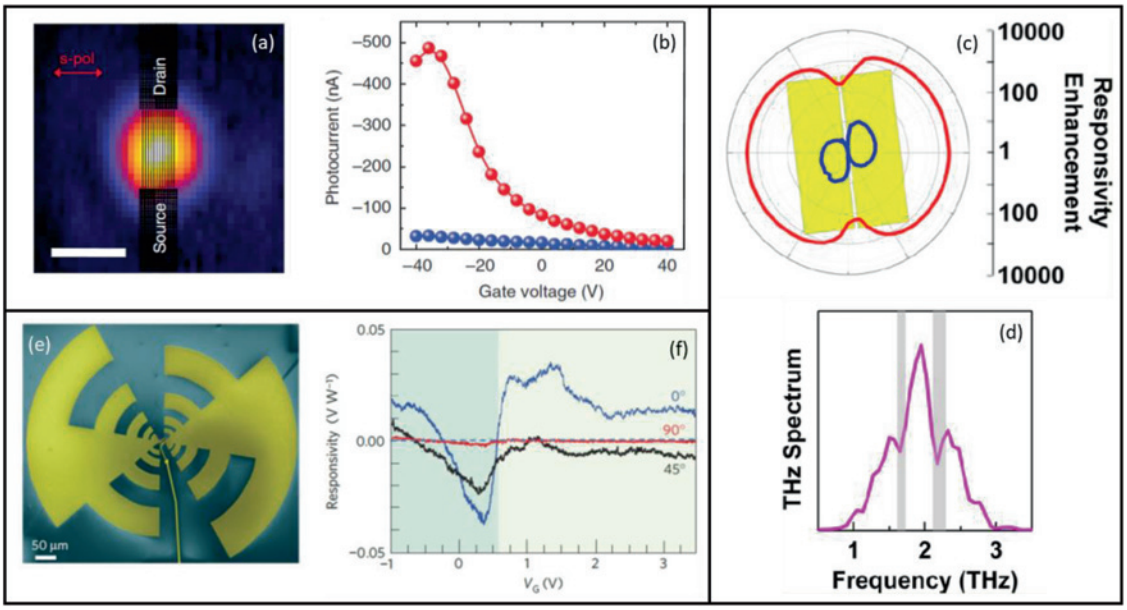

Figure 7: Graphene plasmonic photodetectors. (a) Scanning photocurrent image of a nanoribbon device designed for plasmon-enhanced photodetection near 10 μm wavelength. The scale bar is 30 μm. (b) Photocurrent versus gate voltage measured with the device of (a) for incident light polarized parallel (blue circles) and perpendicular (red circles) to the nanoribbons. (c) Responsivity enhancement of a graphene photo-thermoelectric detector coupled to a metallic double-patch THz antenna, plotted as a function of polarization angle of the incident light. The metallic patches are illustrated by the yellow rectangles. The blue and red traces were measured with the device illuminated from the air above and through an on-chip Si lens, respectively. (d) Thermal radiation spectrum of the same device of (c) under current injection across the two metal patches. The two gray bands indicate water absorption lines. (e) False-color SEM image of an antenna-coupled graphene FET THz photodetector. (f) Responsivity versus gate voltage bias measured with the device of (e) for different angles between the incident-light polarization and the antenna axis. (a), (b): reprinted with permission from ref. [91]. Copyright (2013), Springer Nature. (c), (d): reprinted with permission from ref. [94]. Copyright (2015), American Chemical Society. (e), (f): reprinted with permission from ref. [97]. Copyright (2012), Springer Nature.

polarized perpendicular to the ribbon relative to the orthogonal polarization [Figure 7(b)], consistent with the plasmonic absorption properties of graphene nanoribbons described above. The photocurrent in this device is negative (i. e., the conductivity decreases under illumination), indicating that the dominant photodetection mechanism is the reduction in mobility with increasing electronic temperature. Another mid-infrared device demonstrated more recently [92] consists of an array of graphene nanodisks connected by ultrathin ribbons that provide a sizeable energy barrier (a few 10 meV) for current flow. With this arrangement, photodetection with significantly reduced dark-current noise can be achieved through the plasmon-mediated excitation of hot carriers in the nanodisks with sufficiently high energy to surmount the barriers in the ribbons.

Plasmon-enhanced photodetection has also been reported at THz wavelengths in a photo-thermoelectric device, again using nanoribbons, but in this case connected to different metal contacts (Cr and Au) at the source and drain electrodes [93]. In a somewhat related approach, a metallic double-patch THz antenna (also consisting of different metals) has been used to produce a confined region of high-field enhancement in a continuous sheet of graphene, both for photo-thermoelectric detection and thermal light emission [94]. The enhanced light–matter interaction in this case is related to the fundamental resonance of the antenna slot (rather than GPPs) at a frequency of about 2 THz. An on-chip Si lens is also used to improve the coupling efficiency of externally incident light into the device (and vice versa). The measured polarization-resolved responsivity at resonance is increased by three orders of magnitude in the presence of the antenna [Figure 7(c)]. At the same time, when a large electrical current is driven between the two antenna patches to heat up the graphene electron gas in the slot region, a relatively narrow thermal-radiation spectrum is measured, peaked at the antenna resonance frequency [Figure 7(d)].

A different type of plasmonic THz photodetector that has also been developed with graphene is based on early theoretical work on 2DEGs of traditional semiconductor heterojunctions [95, 96]. In this approach, an incident THz wave is fed to an antenna connected between the source and gate contacts of an FET to produce an AC modulation of the carrier density, and therefore plasmonic oscillations traveling along the device channel. Because of the intrinsically nonlinear electrical transfer characteristics of FETs, this AC signal is then rectified to produce a DC photovoltage across the drain and source contacts. Additionally, if the decay lifetime of the plasmonic oscillations is long compared to the travel time across the channel, a standing wave pattern is produced leading to resonantly enhanced response at discrete frequencies (inversely proportional to the channel width). A graphene photodetector based on this approach has been developed in ref. [97], using a log-periodic circular-toothed antenna connected to a short (~10 μm) CVD-graphene FET [Figure 7(e)]. The observed dependence of responsivity on gate voltage [Figure 7(f)] is in agreement with theoretical expectations for operation in the over-damped (i. e., non-resonantly enhanced) regime. At the same time, the measured room-temperature photovoltage and noise properties (near 0.3 THz) were found to be already suitable for THz imaging applications in realistic settings. The resonant mode of operation has also been reported more recently with an FET device at cryogenic temperatures based on high-mobility exfoliated graphene embedded in h-BN [98].

4 Graphene plasmonics for THz light emission

Compared to the optical modulators and photodetectors just reviewed, research on graphene-based THz light emitters is at present in a much earlier stage. Significant efforts so far have focused on the theoretical proposal and numerical investigation of novel device concepts exploiting various distinctive properties of the graphene 2DEG [13–15, 20–23, 99–101]. Initial experimental progress includes the demonstration of THz radiation from transient photocurrents generated under ultrafast optical excitation, either through quantum interference involving fundamental and second-harmonic pulses [102] or with individual pulses incident on suspended samples [103]. In ref. [104], THz light emission is reported based on a combination of the photon drag effect and optical rectification (enhanced through the excitation of surface plasmons on an underlying metal film). More recently, THz high-harmonic generation with remarkably large conversion efficiency has also been observed [105]. These results substantiate the promise of graphene as a novel THz source material, but at the same time their reliance on optical pumping (rather than electrical injection) is a key limitation for many practical device applications. In the following, we focus on recent work where the underlying radiation mechanism involves (or can be extended to) electrical injection. Once again, graphene plasmonic excitations also play an important role in enhancing the efficiency of these mechanisms.

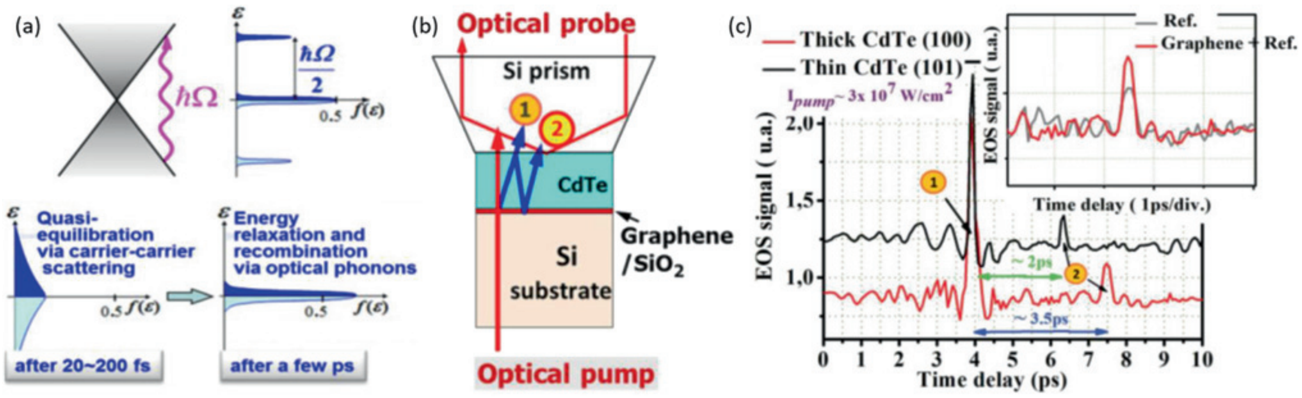

Figure 8: THz interband amplification in graphene. (a) Time evolution of the graphene electronic distribution function *f*(*ε*) after photoexcitation with light of photon energy ħΩ. If intraband equilibration is sufficiently faster than interband recombination, a population inversion can be established. (b) Experimental sample geometry used to investigate THz amplification in optically pumped graphene. (c) Measurement results based on the geometry of (b). The black and red traces show the THz signals measured by electro-optic sampling (EOS) for two different thicknesses of the CdTe crystal, as a function of delay time between the optical pump and probe. The inset shows the THz signal peaks measured after a round-trip inside the crystal [path ② of (b)] with (red) and without (gray) a graphene sheet under the CdTe crystal. The larger peak value of the red trace is an indication of THz amplification by the photoexcited graphene carriers. Reprinted with permission from ref. [109]. Copyright (2012) by the American Physical Society.

4.1 THz interband light emission

In traditional semiconductors, a population inversion across the fundamental energy bandgap can be readily established through the injection of sufficiently high densities of electrons and holes. This behavior is enabled by the ultrafast (sub-picosecond) nature of intraband equilibration compared to interband recombination. As a result, separate quasi-Fermi distributions of electrons and holes can accumulate near the edges of the conduction and valence bands, respectively. Under these conditions, optical gain can be obtained in the spectral range between the bandgap energy and the separation of the electron and hole quasi-Fermi levels. In graphene, where the bandgap energy is zero, such gain would therefore occur at THz frequencies (equivalent to negative dynamic conductivity) [13]. Motivated by these considerations, extensive time-resolved measurements have investigated the relevant relaxation lifetimes in graphene [106–108]. The resulting physical picture, depending on the detailed experimental conditions, is illustrated in Figure 8(a) [109]. Intraband equilibration by carrier-carrier scattering is generally found to occur on a much faster time scale compared to interband recombination (about 100 fs vs. 1–10 ps at room temperature), qualitatively similar to the behavior of traditional gapped semiconductors. The associated carrier temperature dynamics (i. e., cooling to the lattice temperature via phonon emission) is more complex as it depends on the energy range of the initial hot-carrier distribution [108], but usually takes place on an intermediate time scale.

These ideas suggest a potential avenue towards the development of graphene-based THz amplifiers and lasers [13–15, 109–112]. The required carriers could be introduced by optical pumping [13], as illustrated schematically in Figure 8(a). Alternatively, electrons and holes could be injected electrically in a forward-biased *p*-*i*-*n* junction established with a double-gated FET geometry [15], where the two gates are biased with voltages of opposite polarity to introduce carriers of opposite charge in the underlying graphene regions. The amount of population inversion that can be achieved depends on the detailed values of the relevant intraband and interband relaxation lifetimes. In particular, it has been argued that, under conditions of high carrier densities and/or high electronic temperatures, the ability to produce such an inversion is strongly degraded by Auger recombination processes [113]. In any case, even in a fully inverted structure, the maximum achievable gain for single-pass transmission is limited by the universal interband absorption coefficient of graphene (2.3% [114], which is impressive for a single atomic layer but too small for typical device applications). Graphene plasmons once again provide a promising approach to overcome this limitation by virtue of their strong optical confinement and small group velocity, which effectively increase the light–matter overlap and interaction length, respectively. This idea was originally proposed in ref. [14], where extremely large peak gain coefficients of a few

10^4 cm^{-1} were computed for GPPs propagating along a continuous graphene sheet with a reasonable population inversion (on the order of 10^{10}–10^{11} cm^{-2}) and a long but achievable plasmonic scattering lifetime (0.5 ps). More complex structures have also been investigated numerically, including periodic arrays of linear plasmonic nanocavities (defined by multiple parallel electrodes on a continuous sheet), where the peak gain can be further enhanced via coherent phase locking of the plasmonic oscillations in the individual nanocavities [99].

Experimental evidence of THz light amplification in graphene has been reported in refs. 109 and 111, based on time-resolved optical-pump/THz-probe measurements with an exfoliated graphene sample on Si/SiO_2 [Figure 8(b)]. In these experiments, ultrafast infrared pump pulses are used to excite photocarriers in the graphene sheet and, at the same time, produce a THz probe wave by optical rectification in an overlaying CdTe crystal. This THz beam is then detected via electro-optic sampling as it exits the CdTe surface directly [path ① in Figure 8(b)] and after a round-trip inside the crystal [path ②]. The latter signal is found to be significantly stronger in the presence of the graphene sheet compared to a reference device without graphene [Figure 8(c)], suggesting amplification by the graphene carriers. The measured gain, however, is an order of magnitude larger than the aforementioned theoretical limit for interband transitions in graphene. In ref. [111], the authors present additional data suggesting the excitation of GPPs by the THz probe in the same device. This behavior could explain the large measured gain, but it is still not clear how THz photons may couple in and out of surface plasmons in the continuous unpatterned graphene sheets used in these experiments. A more recent publication also reports the measurement of THz radiation from an electrically driven dual-gate graphene FET integrated with a distributed-feedback cavity, including a rather weak and spectrally narrow emission feature at 100 K [112]. This observation may be interpreted as indicative of lasing, although additional data will be required for a more conclusive claim.

4.2 THz light emission from current-driven plasmonic oscillations

A completely different approach for THz light emission in graphene relies on the generation of hot carriers under current injection and their subsequent energy relaxation through the excitation of GPPs [115]. Free-space THz radiation can then be emitted by the resulting collective oscillations of the graphene electron gas. This idea was originally investigated in early work with grating-coupled 2DEGs in traditional semiconductor heterojunctions, such as Si/SiO_2 and GaAs/AlGaAs [40, 116, 117]. Pronounced THz emission peaks were measured with these systems, but only at cryogenic temperatures, which were used to study hot-carrier effects and plasmonic dispersion properties. The use of graphene for this application is once again attractive because of its exceptional transport properties, allowing for reduced plasmonic damping and thus particularly narrow emission spectra even at ambient temperature [118]. Graphene is also an ideal materials system for the excitation of hot carriers, by virtue of its low electronic heat capacity and weak electron-phonon coupling. Prior work has already established its promise as a stable and efficient thermal emitter at mid-infrared [119, 120] and visible [121] wavelengths. Additionally, the strong confinement of graphene plasmons in the supporting 2DEG is favorable to enhance plasmon generation via hot-carrier decay. In fact, it has been suggested that the latter process in graphene can become remarkably efficient and lead to unusual effects such as the generation of plasmonic shockwaves [122].

The initial experimental demonstration of current-driven THz light emission from graphene plasmonic oscillations is summarized in Figure 9(a)–(c) [115]. The devices used in this work consist of CVD graphene nanoribbons patterned on a back-gated Si/SiO_2 FET, similar to the structure of Figure 2(a). Perpendicular "bridge" sections are also introduced to connect neighboring ribbons to one another, in order to minimize the impact of material defects and cracks on the current flow through the entire device [Figure 9(a)]. Figure 9(b) shows a representative emission spectrum measured with a device at a substrate temperature T_{base} of 80 K, for an input electrical power P_{in} of 0.2 W (determined by the applied source-drain current and voltage). This trace is normalized to the emission spectrum of the same sample gated at charge neutrality, so as to fully highlight the plasmonic contribution. A sharp peak with quality factor of about four is observed, centered near the nanoribbon plasmonic resonance frequency $\nu_{pl} \approx 8$ THz. To illustrate the geometrical and electrostatic tunability of these devices, the symbols in Figure 9(c) show the peak emission frequencies measured with two samples of different ribbon width w (530 and 810 nm) as a function of carrier density N. The solid and dashed lines are computed, respectively, with the analytical expression for the nanoribbon resonance frequency ν_1 of Eq. (2) and via FDTD simulations. Excellent agreement with the experimental data is obtained with both analytical and numerical modeling, and altogether these two devices can cover a rather broad spectral range from about 4 to 8 THz.

In the work of ref. [115], these emission spectra could only be resolved up to a maximum substrate base temperature T_{base} of about 190 K. The output power levels measured around liquid-nitrogen temperature are on the order of a few nW, corresponding to a rather low wall-plug efficiency $\Delta P_{out}/P_{in} \sim 10^{-8}$. In order to understand the key factors limiting these performance metrics, and to identify possible avenues for improvement, we present a simple theoretical model of the underlying emission mechanism. The radiation spectra under study can be described as thermal emission resonantly enhanced by the excitation of surface plasmons. Therefore, consistent with Kirchhoff's law of thermal radiation for a collection of resonant nanoparticles [123], their power density per unit area per unit frequency $\rho_{out}(\nu, T)$ is given by Planck's formula for blackbody emission $\rho_{bb}(\nu, T) = (2\pi h\nu^3/c^2)/[\exp(h\nu/k_B T) - 1]$ multiplied by the nanoparticle absorption efficiency. The absorption efficiency is defined as the ratio between absorption cross-section and physical surface area and, importantly, can be well above one at frequencies near a nanoparticle absorption resonance. For the devices of Figure 9, it can be written as $\eta_{GPP}(\nu) = \alpha_{GPP}(\nu)S_{tot}/S_{gr}$, where S_{gr} is the graphene surface area, S_{tot} is the total device area (including both graphene nanoribbons and the empty spaces in between), and $\alpha_{GPP}(\nu)$ is the fraction of light incident on the entire device that is absorbed by the plasmonic oscillations. The plasmonic output power can then be computed as $P_{out} = \int d\nu \rho_{out}(\nu, T)S_{gr}$ and, for a sufficiently narrow plasmonic absorption peak (of center frequency ν_{pl} and FWHM linewidth $\delta\nu$), it can be approximated as $P_{out} \approx \rho_{out}(\nu_{pl}, T)S_{gr}\delta\nu$. With this formulation, we finally obtain the following expression for the wall-plug efficiency:

$$\Delta P_{out}/P_{in} = \langle \eta_{GPP}(\nu_{pl})\rangle[\rho_{bb}(\nu_{pl}, T_{el}) - \rho_{bb}(\nu_{pl}, T_{base})]\delta\nu/p_{in}. \tag{4}$$

Here, ΔP_{out} is the increase in plasmonic output power produced by the injected current; T_{el} is the 2DEG temperature under bias, which can be estimated from the input power density $p_{in} = P_{in}/S_{gr}$ using available analytical models [124–126]; and the brackets $\langle\rangle$ indicate averaging over two orthogonal incident polarizations, which is required since the Planck's formula for ρ_{bb} describes unpolarized radiation.

The key conclusion that emerges from this analysis is that all the design prescriptions described above for maximizing the plasmonic absorption strength $\alpha_{GPP}(\nu_{pl})$ are also beneficial in the context of the THz light-emitting devices of Figure 9. In addition, since the output power ΔP_{out} of Eq. (4) is proportional to the absorption efficiency η_{GPP}, further enhancements can be achieved by optimizing the geometrical factor S_{tot}/S_{gr}. To illustrate the corresponding margins for improvement, in Figure 9(d) we plot the polarization-averaged peak absorption efficiency $\langle\eta_{GPP}(\nu_{pl})\rangle$ computed by FDTD simulations as a function of graphene mobility for two different structures. The blue squares correspond to the device of Figure 9(b). Based on these simulation results combined with the relevant experimental parameters ($S_{tot} = 190 \times 150\ \mu m^2$, $S_{tot}/S_{gr} = 1.9$, $N = 5.4 \times 10^{12}\ cm^{-2}$, $T_{base} = 80$ K, $P_{in} = 0.2$ W, and

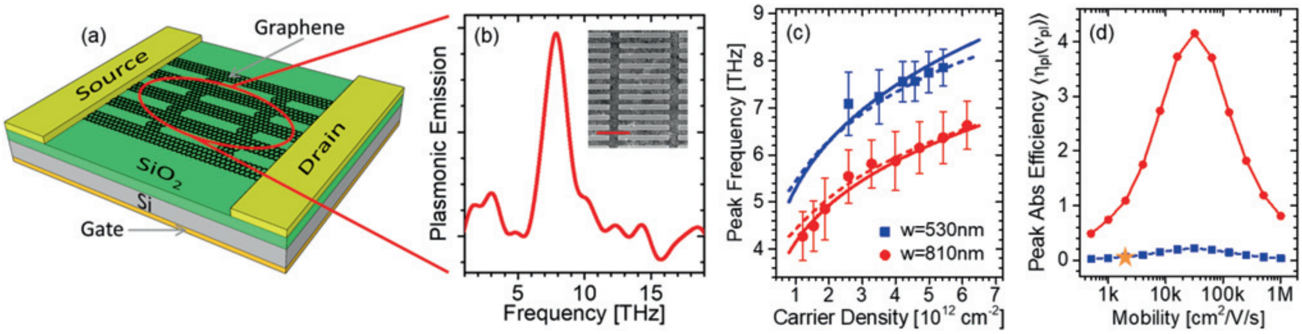

Figure 9: THz light emission from plasmonic oscillations in graphene nanoribbons. (a) Schematic device structure. (b) Measured radiation spectrum of a sample with 530 nm-wide ribbons and 1.0 μm center-to-center spacing at a carrier density $N = 5.4 \times 10^{12}\ cm^{-2}$, normalized to the spectrum at the charge neutrality point. The base temperature is 80 K and the input electrical power 0.2 W. Inset: top-view SEM image. The scale bar is 3 μm. (c) Symbols: peak emission frequencies of the spectra measured with two devices of different nanoribbon width w. Solid lines: numerical fits to the analytical expression of Eq. (2) with a single fitting parameter (the reflection phase φ_r, for which a value of 0.27π is estimated). Dashed lines: resonance frequencies computed by FDTD simulations. (d) Polarization-averaged peak absorption efficiency versus mobility for two different plasmonic THz emitters. The blue squares correspond to the device of (b). The red circles correspond to the vertical-cavity nanoribbon device structure of Figure 6 (with 530 nm ribbon width and 4.4 μm spacing) at $N = 6.5 \times 10^{12}\ cm^{-2}$. In each structure, the nanoribbon fill factor is optimized for maximum absorption efficiency. The star symbol indicates the operating point for the experimental data of (b). (a)–(c): reprinted with permission from ref. [115]. Copyright (2019), American Chemical Society.

$\mu = 2{,}000\ \mathrm{cm^2/Vs}$ as indicated by the star in the figure), we compute a plasmonic output power ΔP_{out} of 5.4 nW and a wall-plug efficiency $\Delta P_{\mathrm{out}}/P_{\mathrm{in}}$ of 3×10^{-8}. This estimate is in reasonably good agreement with the power extrapolated from the experimental data of Figure 9(b) (3.4 nW [115]), which substantiates the validity of the present model. The red circles in Figure 9(d) refer to a similar nanoribbon device on an optimized Salisbury-screen substrate (the structure of Figure 6). At any fixed mobility, an increase in absorption efficiency by a factor of about 20 is obtained over the reference design represented by the blue squares. At the optimal mobility for critical coupling [again ~30,000 $\mathrm{cm^2/Vs}$ in Figure 9(d)], the calculated absorption efficiency of this vertical-cavity device is nearly 70 times larger than in the measurements of Figure 9(b).

Further improvements can be expected by using higher doping and DLG samples, as discussed in Section 2.4. The use of graphene nanostructures featuring a polarization-independent plasmonic response is also beneficial to increase the polarization-averaged peak absorption. Suitable designs include circular or slightly elliptical disks connected to one another by narrow ribbons to enable gating and current flow [92]. The graphene plasmonic oscillators could also be integrated with additional THz antennas in order to increase their radiative decay rate Γ_{rad}, and therefore decrease the optimal mobility for critical coupling to values accessible with large-area CVD graphene. As a result, the absorption strength could be further enhanced, similar to the aforementioned prior work on optical modulators [68, 69]. Through a combination of these design prescriptions, THz output powers approaching the mW range may be achievable with large (but realistic [119, 121]) input electrical powers of about 100 W delivered to a total device area of a few $\mathrm{mm^2}$. Combined with its relatively simple manufacturing and broadband tunability, the resulting technology would then be quite appealing as a way to address the present lack of practical THz radiation sources.

5 Conclusion

In summary, we have reviewed the basic physics and THz device applications of plasmonic excitations in graphene nanostructures. These resonances provide an effective way to enhance light–matter interactions in a highly tunable fashion, although the magnitude of the enhancement strongly depends on the sample mobility and surrounding dielectric environment. While ultrahigh mobilities are accessible, even at room temperature, in suspended or h-BN-embedded graphene, the resulting devices are currently limited by exceedingly small dimensions, particularly for long-wavelength photonic device applications. In contrast, the impact of the surrounding environment on the plasmonic absorption strength provides a wealth of design opportunities that can be addressed with available nanophotonic technologies, and significant progress in this direction has already been reported [68–71]. In the context of THz optoelectronics, the distinctive properties of graphene plasmons are particularly well suited for application to optical modulators, and initial work suggests that competitive devices in terms of all the key performance metrics (modulation depth, drive voltage, speed) could be developed with a focused engineering effort [68, 69, 86]. Promising graphene photodetectors based on plasmonic effects have also been demonstrated [91–94, 97, 98] and even employed in a prototype THz imaging setup [97]. On the other hand, significantly less progress has been reported so far in the area of THz radiation sources, which perhaps mirrors the great challenges encountered in the development of such devices based on other materials systems. The recent results reviewed in Section 4 are promising, but extensive additional work will be required to fully assess their potential for a direct technological impact.

If adequate performance levels can be achieved, all of these THz devices would be quite compelling for several reasons, common to other graphene technologies: they can be manufactured with relatively simple and inexpensive processes (e. g., not requiring any complex heteroepitaxial growth), are directly compatible with a wide range of substrates (including Si-based microelectronic systems), and can provide extreme size miniaturization. These properties are particularly attractive for the development of large-scale THz integrated circuits, which currently are limited to operation frequencies below 1 THz and/or extremely small component counts [127, 128]. In turn, these systems could benefit many established applications of THz devices (e. g., imaging and sensing for security screening, industrial inspection, and medical diagnostics) and possibly contribute to the emergence of new ones, such as on-chip processing of optical data at THz speeds. The investigation and development of the underlying device functionalities are also important from a fundamental standpoint, as a way to shed new light on the rich interplay between hot carriers, plasmons, and photons in 2D nanostructures.

Acknowledgments: This work was partly supported by the National Science Foundation under Grant #DMR-1308659. The FDTD simulations were performed using the Shared Computing Cluster facility at Boston University.

References

[1] M. Lee and M. C. Wanke, “Searching for a solid-state terahertz technology,” *Science*, vol. 316, pp. 64, 2007, https://doi.org/10.1126/science.1141012.

[2] D. M. Mittleman, “Frontiers in terahertz sources and plasmonics,” *Nat. Photon.*, vol. 7, pp. 666, 2013, https://doi.org/10.1038/nphoton.2013.235.

[3] S. S. Dhillon, M. S. Vitiello, E. H. Linfield, et al., “The 2017 terahertz science and technology roadmap,” *J. Phys. D: Appl. Phys.*, vol. 50, p. 043001, 2017, https://doi.org/10.1088/1361-6463/50/4/043001.

[4] P. U. Jepsen, D. G. Cooke, and M. Koch, “Terahertz spectroscopy and imaging – Modern techniques and applications,” *Laser Photon. Rev.*, vol. 5, pp. 124–166, 2011, https://doi.org/10.1002/lpor.201000011.

[5] X. Yang, X. Zhao, K. Yang, et al., “Biomedical applications of terahertz spectroscopy and imaging,” *Trends Biotechnol.*, vol. 34, pp. 810–824, 2016, https://doi.org/10.1016/j.tibtech.2016.04.008.

[6] B. S. Williams, “Terahertz quantum-cascade lasers,” *Nat. Photon.*, vol. 1, pp. 517–525, 2007, https://doi.org/10.1038/nphoton.2007.166.

[7] R. Paiella, “Quantum cascade lasers,” in *Comprehensive Semiconductor Science & Technology*. P. Bhattacharya, R. Fornari, and H. Kamimura, Eds., Vol. 5. Amsterdam, Elsevier, 2011, pp. 683–723.

[8] N. M. Burforda, M. O. El-Shenawee, 2017. Review of terahertz photoconductive antenna technology. Opt. Eng. 56, 10901. https://doi.org/10.1117/1.oe.56.1.010901.

[9] P. Tassin, T. Koschny, C. M. Soukoulis, 2013. Graphene for terahertz applications. Science 341, 620–621. https://doi.org/10.1126/science.1242253.

[10] T. Low, P. Avouris, 2014. Graphene plasmonics for terahertz to mid-infrared applications. ACS Nano 8, 1086–1101. https://doi.org/10.1021/nn406627u.

[11] A. Tredicucci and M. S. Vitiello, “Device concepts for graphene-based terahertz photonics,” *IEEE J. Select. Topics Quantum Electron.*, vol. 20, p. 8500109, 2014, https://doi.org/10.1109/JSTQE.2013.2271692.

[12] R. Wang, X.-G. Ren, Z. Yan, Jiang, L.-J., Sha, W. E. I., G.-C. Shan, 2019. Graphene based functional devices: A short review. Front. Phys. 14, 13603. https://doi.org/10.1007/s11467-018-0859-y.

[13] V. Ryzhii, M. Ryzhii, and T. Otsuji, “Negative dynamic conductivity of graphene with optical pumping,” J. Appl. Phys., vol. 101, p. 083114, 2007, https://doi.org/10.1063/1.2717566.

[14] F. Rana, 2008. Graphene terahertz plasmon oscillators. IEEE Trans. Nanotechnol. 7, 91. https://doi.org/10.1109/TNANO.2007.910334.

[15] V. Ryzhii, M. Ryzhii, V. Mitin, T. Otsuji, 2011. Toward the creation of terahertz graphene injection laser. J. Appl. Phys. 110, 094503. https://doi.org/10.1063/1.3657853.

[16] K. I. Bolotin, K. J.Sikes, J. Hone, H. L. Stormer, P. Kim, 2008. Temperature-dependent transport in suspended graphene. Phys. Rev. Lett. 101, 96802. https://doi.org/10.1103/PhysRevLett.101.096802.

[17] X. Du, I. Skachko, A. Barker, Andrei, E. Y., 2008. Approaching ballistic transport in suspended graphene. Nat. Nanotechnol. 3, 491. https://doi.org/10.1038/nnano.2008.199.

[18] A. S. Mayorov, R. V. Gorbachev, S. V. Morozov, et al., 2011. Micrometer-scale ballistic transport in encapsulated graphene at room temperature. Nano Lett. 11, 2396. https://doi.org/10.1021/nl200758b.

[19] L. Wang, I. Meric, P. Y. Huang, et al., 2013. One-dimensional electrical contact to a two-dimensional material. Science 342, 614–617. https://doi.org/10.1126/science.1244358.

[20] V. Ryzhii, M. Ryzhii, V. Mitin, and M. S. Shur, “Graphene tunneling transit-time terahertz oscillator based on electrically induced p–i–n junction,” *Appl. Phys. Express*, vol. 2, p. 034503, 2009, https://doi.org/10.1143/APEX.2.034503.

[21] K. Tantiwanichapan, J. DiMaria, S. N. Melo, and R. Paiella, “Graphene electronics for terahertz electron-beam radiation,” *Nanotechnology*, vol. 24, p. 375205, 2013, https://doi.org/10.1088/0957-4484/24/37/375205.

[22] K. Tantiwanichapan, X. Wang, A. K. Swan, and R. Paiella, “Graphene on nanoscale gratings for the generation of terahertz Smith-Purcell radiation,” *Appl. Phys. Lett.*, vol. 105, p. 241102, 2014, https://doi.org/10.1063/1.4904264.

[23] K. Tantiwanichapan, A. K. Swan, and R. Paiella, “One-dimensional carbon nanostructures for terahertz electron-beam radiation,” *Phys. Rev. B*, vol. 93, p. 235416, 2016, https://doi.org/10.1103/PhysRevB.93.235416.

[24] A. N. Grigorenko, M. Polini, and K. S. Novoselov, “Graphene plasmonics,” *Nat. Photon.*, vol. 6, pp. 749–758, 2012, https://doi.org/10.1038/nphoton.2012.262.

[25] F. J. García de Abajo, 2014. Graphene plasmonics: challenges and opportunities. ACS Photon. 1, 135–152. https://doi.org/10.1021/ph400147y.

[26] S. Xiao, X. Zhu, B. Li, Mortensen, N. A., 2016. Graphene-plasmon polaritons: From fundamental properties to potential applications. Front. Phys. 11, 117801. https://doi.org/10.1007/s11467-016-0551-z.

[27] Q. Guo, C. Li, B. Deng, S. Yuan, F. Guinea, and F. Xia, “Infrared nanophotonics based on graphene plasmonics,” ACS Photon., vol. 4, pp. 2989–2999, 2017, https://doi.org/10.1021/acsphotonics.7b00547.

[28] A. Vakil, N. Engheta, 2011. Transformation optics using graphene. Science 332, 1291. https://doi.org/10.1126/science.1202691.

[29] R. Frisenda, E. Navarro-Moratalla, P. Gant, et al., 2018. Recent progress in the assembly of nanodevices and van der Waals heterostructures by deterministic placement of 2D materials. Chem. Soc. Rev. 47, 53. https://doi.org/10.1039/C7CS00556C.

[30] S. A. Maier. *Plasmonics: Fundamentals and Applications*. New York, Springer, 2007.

[31] J. Gómez Rivas, M. Kuttge, P. Haring Bolivar, H. Kurz, and J. A. Sánchez-Gil, “Propagation of surface plasmon polaritons on semiconductor gratings,” *Phys. Rev. Lett.*, vol. 93, p. 256804, 2004, https://doi.org/10.1103/PhysRevLett.93.256804.

[32] S. J. Allen, D. C. Tsui, and R. A. Logan, “Observation of 2-dimensional plasmon in silicon inversion layers,” *Phys. Rev. Lett.*, vol. 38, pp. 980–983, 1977, https://doi.org/10.1103/PhysRevLett.38.980.

[33] D. N. Basov, M. M. Fogler, and F. J. García de Abajo, “Polaritons in van der Waals materials,” *Science*, vol. 354, p. 1992, 2016, https://doi.org/10.1126/science.aag1992.

[34] E. H. Hwang and S. Das Sarma, “Dielectric function, screening, and plasmons in two-dimensional graphene,” *Phys. Rev. B*, vol.

75, p. 205418, 2007, https://doi.org/10.1103/PhysRevB.75.205418.

[35] M. Jablan, H. Buljan, and M. Soljačić, "Plasmonics in graphene at infrared frequencies," *Phys. Rev. B*, vol. 80, p. 245435, 2009, https://doi.org/10.1103/PhysRevB.80.245435.

[36] N. Sule, K. J. Willis, S. C. Hagness, and I. Knezevic, "Terahertz-frequency electronic transport in graphene," *Phys. Rev. B*, vol. 90, p. 045431, 2014, https://doi.org/10.1103/PhysRevB.90.045431.

[37] F. Stern, "Polarizability of a two-dimensional electron gas," *Phys. Rev. Lett.*, vol. 18, p. 546, 1967, https://doi.org/10.1103/PhysRevLett.18.546.

[38] A. Woessner, M. B. Lundeberg, Y. Gao, et al., "Highly confined low-loss plasmons in graphene–boron nitride heterostructures," *Nat. Mater.*, vol. 14, pp. 421–425, 2014, https://doi.org/10.1038/nmat4169.

[39] K. M. Daniels, M. M. Jadidi, A. B. Sushkov, et al., "Narrow plasmon resonances enabled by quasifreestanding bilayer epitaxial graphene," *2D Mater.*, vol. 4, p. 025034, 2017, https://doi.org/10.1088/2053-1583/aa5c75.

[40] N. Okisu, Y. Sambe, and T. Kobayashi, "Far-infrared emission from two-dimensional plasmons in AlGaAs/GaAs heterointerfaces," *Appl. Phys. Lett.*, vol. 48, pp. 776–778, 1986, https://doi.org/10.1063/1.114333.

[41] J. Chen, M. Badioli, P. Alonso-González, et al., 2012. Optical nano-imaging of gate-tunable graphene plasmons. Nature 487, 77–81. https://doi.org/10.1038/nature11254.

[42] Z. Fei, A. S. Rodin, G. O. Andreev, et al., 2012. Gate-tuning of graphene plasmons revealed by infrared nano-imaging. Nature 487, 82–85. https://doi.org/10.1038/nature11253.

[43] Z. Fei, A. S. Rodin, W. Gannett, et al., 2013. Electronic and plasmonic phenomena at graphene grain boundaries. Nat. Nanotechnol. 8, 821. https://doi.org/10.1038/nnano.2013.197.

[44] Q. Xu, T. Ma, M. Danesh, et al., "Effects of edge on graphene plasmons as revealed by infrared nanoimaging," Light: Sci. Appl., vol. 6, p. e16204, 2017, https://doi.org/10.1038/lsa.2016.204.

[45] L. Ju, B. Geng, J. Horng, et al., 2011. Graphene plasmonics for tunable terahertz metamaterials. Nat. Nanotechnol. 6, 630–634. https://doi.org/10.1038/nnano.2011.146.

[46] H. Yan, T. Low, W. Zhu, et al., 2013. Damping pathways of mid-infrared plasmons in graphene nanostructures. Nat. Photon. 7, 394–399. https://doi.org/10.1038/nphoton.2013.57.

[47] V. W. Brar, M. S. Jang, M. Sherrott, J. J. Lopez, and H. A. Atwater, "Highly confined tunable mid-infrared plasmonics in graphene nanoresonators," Nano Lett., vol. 13, pp. 2541–2547, 2013, https://doi.org/10.1021/nl400601c.

[48] I. J. Luxmoore, C. H. Gan, P. Q. Liu, et al., "Strong coupling in the far-infrared between graphene plasmons and the surface optical phonons of silicon dioxide," ACS Photon., vol. 1, pp. 1151–1155, 2014, https://doi.org/10.1021/ph500233s.

[49] M. M. Jadidi, A. B. Sushkov, R. L. Myers-Ward, et al., 2015. Tunable terahertz hybrid metal–graphene plasmons. Nano Lett. 15, 7099. https://doi.org/10.1021/acs.nanolett.5b03191.

[50] H. Yan, X. Li, B. Chandra, et al., "Tunable infrared plasmonic devices using graphene/insulator stacks," *Nat. Nanotechnol.*, vol. 7, pp. 330–334, 2012, https://doi.org/10.1038/nnano.2012.59.

[51] Z. Fang, S. Thongrattanasiri, A. Schlather, et al., 2013. Gated tunability and hybridization of localized plasmons in nanostructured graphene. ACS Nano 7, 2388–2395. https://doi.org/10.1021/nn3055835.

[52] X. Zhu, W. Wang, W. Yan, et al., 2014. Plasmon–phonon coupling in large-area graphene dot and antidot arrays fabricated by nanosphere lithography. Nano Lett. 14, 2907–2913. https://doi.org/10.1021/nl500948p.

[53] X. Zhu, W. Yan, Jepsen, P.U., O. Hansen, Mortensen, N.A., S. Xiao, 2013. Experimental observation of plasmons in a graphene monolayer resting on a two-dimensional subwavelength silicon grating. Appl. Phys. Lett. 102, 131101. https://doi.org/10.1063/1.4799173.

[54] W. Gao, G. Shi, Z. Jin, et al., 2013. Excitation and active control of propagating surface plasmon polaritons in graphene. Nano Lett. 13, 3698–3702. https://doi.org/10.1016/j.rinp.2017.02.006.

[55] J. Song, L. Zhang, Xue, Y., et al., 1986–1992, 2016. Efficient excitation of multiple plasmonic modes on three-dimensional graphene: an unexplored dimension. ACS Photon. 3. https://doi.org/10.1021/acsphotonics.6b00566.

[56] K. Tantiwanichapan, X. Wang, H. Durmaz, Y. Li, Swan, A. K., R. Paiella, 2017. Graphene terahertz plasmons: a combined transmission spectroscopy and Raman microscopy study. ACS Photon. 4, 2011–2017. https://doi.org/10.1021/acsphotonics.7b00384.

[57] K. Y. M. Yeung, J. Chee, H. Yoon, Y. Song, J. Kong, D. Ham, 2014. Far-infrared graphene plasmonic crystals for plasmonic band engineering," Nano Lett 14, 2479–2484. https://doi.org/10.1021/nl500158y.

[58] P. Q. Liu, F. Valmorra, C. Maissen, J. Faist, 2015. Electrically tunable graphene anti-dot array terahertz plasmonic crystals exhibiting multi-band resonances. Optica 2, 135–140. https://doi.org/10.1364/OPTICA.2.000135.

[59] A. Y. Nikitin, T. Low, L. Martin-Moreno, 2014. Anomalous reflection phase of graphene plasmons and its influence on resonators. Phys. Rev. B 90, 41407. https://doi.org/10.1103/PhysRevB.90.041407.

[60] J. H. Kang, S. Wang, Z. Shi, W. Zhao, E. Yablonovitch, and F. Wang, "Goos-Hänchen shift and even–odd peak oscillations in edge reflections of surface polaritons in atomically thin crystals," Nano Lett., vol. 17, pp. 1768–1774, 2017, https://doi.org/10.1021/acs.nanolett.6b05077.

[61] J. Christensen, A. Manjavacas, S. Thongrattanasiri, Koppens, F.H.L., García de Abajo, F.J., 2012. Graphene plasmon waveguiding and hybridization in individual and paired nanoribbons. ACS Nano 6, 431–440. https://doi.org/10.1021/nn2037626.

[62] J. E. Lee, G. Ahn, J. Shim, Y. S. Lee, S. Ryu, 2012. Optical separation of mechanical strain from charge doping in graphene. Nature Comm. 3, 1024. https://doi.org/10.1038/ncomms2022.

[63] O. M. Nayfeh, A. G. Birdwell, C. Tan, et al., 2013. Increased mobility for layer-by-layer transferred chemical vapor deposited graphene/boron-nitride thin films. Appl. Phys. Lett. 102, 103115. https://doi.org/10.1063/1.4794533.

[64] S. J. Kim, T. Choi, B. Lee, et al., 2015. Ultraclean patterned transfer of single-layer graphene by recyclable pressure sensitive adhesive films. Nano Lett. 15, 3236–3240. https://doi.org/10.1021/acs.nanolett.5b00440.

[65] D. Rodrigo, A. Tittl, O. Limaj, F. J.García de Abajo, V. Pruneri, H. Altug, 2017. Double-layer graphene for enhanced tunable infrared plasmonics. Light: Sci. Appl. 6, e16277. https://doi.org/10.1038/lsa.2016.277.

[66] H. A. Haus. *Waves and Fields in Optoelectronics*. Englewood Cliffs, NJ, Prentice-Hall, 1984.

[67] J. Yoon, K. H. Seol, S. H. Song, and R. Magnusson, “Critical coupling in dissipative surface-plasmon resonators with multiple ports,” *Opt. Express*, vol. 18, p. 25702, 2010, https://doi.org/10.1364/OE.18.025702.

[68] P. Q. Liu, I. J. Luxmoore, S. A. Mikhailov, et al., “Highly tunable hybrid metamaterials employing split-ring resonators strongly coupled to graphene surface plasmons,” *Nat. Commun.*, vol. 6, pp. 8969, 2015, https://doi.org/10.1038/ncomms9969.

[69] S. Kim, M. S. Jang, V. W. Brar, K. W. Mauser, L. Kim, and H. A. Atwater, “Electronically tunable perfect absorption in graphene,” *Nano Lett.*, vol. 18, pp. 971–979, 2018, https://doi.org/10.1021/acs.nanolett.7b04393.

[70] S. Thongrattanasiri, F. H. L. Koppens, F. J. García de Abajo, 2012. Complete optical absorption in periodically patterned graphene. Phys. Rev. Lett. 108, 47401. https://doi.org/10.1103/physrevlett.108.047401.

[71] R. Alaee, M. Farhat, C. Rockstuhl, F. Lederer, 2012. A perfect absorber made of a graphene micro-ribbon metamaterial. Opt. Express 20, 28017–28024. https://doi.org/10.1364/OE.20.028017.

[72] X. Yao, M. Tokman, and A. Belyanin, “Efficient nonlinear generation of THz plasmons in graphene and topological insulators,” Phys. Rev. Lett., vol. 112, 2014, p. 055501, https://doi.org/10.1103/PhysRevLett.112.055501.

[73] B. Yao, Y. Liu, S. W. Huang, et al., 2018. Broadband gate-tunable terahertz plasmons in graphene heterostructures. Nat. Photon. 12, 22–28. https://doi.org/10.1038/s41566-017-0054-7.

[74] Y. Li, H. Yan, D. B. Farmer, et al., 2014. Graphene plasmon enhanced vibrational sensing of surface-adsorbed layers. Nano Lett. 14, 1573–1577. https://doi.org/10.1021/nl404824w.

[75] D. Rodrigo, O. Limaj, D. Janner, et al., 2015. Mid-infrared plasmonic biosensing with graphene. Science 349, 165–168. https://doi.org/10.1126/science.aab2051.

[76] B. Sensale-Rodriguez, R. S. Yan, M. M. Kelly, et al., 2012. Broadband graphene terahertz modulators enabled by intraband transitions. Nat. Commun. 3, 780. https://doi.org/10.1038/ncomms1787.

[77] L. Ren, Q. Zhang, J. Yao, et al., 2012. Terahertz and infrared spectroscopy of gated large-area graphene. Nano Lett. 12, 3711. https://doi.org/10.1021/nl301496r.

[78] P. Weis, Garcia-Pomar, J. L., M. Hoh, B. Reinhard, A. Brodyanski, M. Rahm, 2012. Spectrally wide-band terahertz wave modulator based on optically tuned graphene. ACS Nano 6, 9118–9124. https://doi.org/10.1021/nn303392s.

[79] S. H. Lee, M. Choi, T. T. Kim, et al., 2012. Switching terahertz waves with gate-controlled active graphene metamaterials. Nat. Mater. 11, 936–941. https://doi.org/10.1038/nmat3433.

[80] S. F. Shi, B. Zeng, H. L. Han, et al., “Optimizing broadband terahertz modulation with hybrid graphene/metasurface structures,” *Nano Lett.*, vol. 15, pp. 372–377, 2015, https://doi.org/10.1021/nl503670d.

[81] D. S. Jessop, S. J. Kindness, L. Xiao, et al., “Graphene based plasmonic terahertz amplitude modulator operating above 100 MHz,” *Appl. Phys. Lett.*, vol. 108, p. 171101, 2016, https://doi.org/10.1063/1.4947596.

[82] M. Mittendorff, S. Li, and T. E. Murphy, “Graphene-based waveguide-integrated terahertz modulator,” *ACS Photon.*, vol. 4, pp. 316–321, 2017, https://doi.org/10.1021/acsphotonics.6b00751.

[83] M. Mittendorff, S. Winner, J. Kamann, et al., “Ultrafast graphene-based broadband THz detector,” *Appl. Phys. Lett.*, vol. 103, p. 021113, 2013, https://doi.org/10.1063/1.4813621.

[84] X. Cai, A. B. Sushkov, R. J. Suess, et al., “Sensitive room-temperature terahertz detection via the photothermoelectric effect in graphene,” *Nat. Nanotechnol.*, vol. 9, pp. 814–819, 2014, https://doi.org/10.1038/nnano.2014.182.

[85] D. Yadav, S. Boubanga Tombet, T. Watanabe, S. Arnold, V. Ryzhii, and T. Otsuji, “Terahertz wave generation and detection in double-graphene layered van der Waals heterostructures,” *2D Mater.*, vol. 3, p. 045009, 2016, https://doi.org/10.1088/2053-1583/3/4/045009.

[86] S. Chakraborty, O. P. Marshall, T. G. Folland, Y. J. Kim, A. N. Grigorenko, K. S. Novoselov, 2016. Gain modulation by graphene plasmons in aperiodic lattice lasers. Science 351, 246–248. https://doi.org/10.1126/science.aad2930.

[87] W. W. Salisbury, “Absorbent body for electromagnetic waves,” U.S. Patent 1952, 2,599,944.

[88] F. H. L. Koppens, T. Mueller, P. Avouris, A. C. Ferrari, M. S. Vitiello, M. Polini, 2014. Photodetectors based on graphene, other two-dimensional materials and hybrid systems. Nat. Nanotechnol. 9, 780–793. https://doi.org/10.1038/nnano.2014.215.

[89] J. Yan, Kim, M. H., Elle, J. A., et al., 2012. Dual-gated bilayer graphene hot-electron bolometer. Nature Nanotechnol. 7, 472–478. https://doi.org/10.1038/nnano.2012.88.

[90] M. L. Brongersma, N. J. Halas, P. Nordlander, 2015. Plasmon induced hot carrier science and technology. Nat. Nanotechnol. 10, 25–34. https://doi.org/10.1038/nnano.2014.311.

[91] M. Freitag, T. Low, W. Zhu, H. Yan, F. Xia, P. Avouris, 1951, 2013. Photocurrent in graphene harnessed by tunable intrinsic plasmons. Nat. Commun. 4. https://doi.org/10.1038/ncomms2951.

[92] Q. Guo, R. Yu, C. Li, et al., 2018. Efficient electrical detection of mid-infrared graphene plasmons at room temperature. Nat. Mater. 17, 986–992. https://doi.org/10.1038/s41563-018-0186-2.

[93] X. Cai, A. B. Sushkov, M. M. Jadidi, et al., 2015. Plasmon-enhanced terahertz photodetection in graphene. Nano Lett. 15, 4295–4302. https://doi.org/10.1021/acs.nanolett.5b00137.

[94] J. Tong, M. Muthee, S. Y. Chen, S. K. Yngvesson, J. Yan, 2015. Antenna enhanced graphene THz emitter and detector. Nano Lett. 15, 5295–5301. https://doi.org/10.1021/acs.nanolett.5b01635.

[95] M. Dyakonov, M. Shur, 1993. Shallow water analogy for a ballistic field effect transistor: New mechanism of plasma wave generation by dc current. Phys. Rev. Lett. 71, 2465–2468. https://doi.org/10.1103/physrevlett.71.2465.

[96] M. Dyakonov, M. Shur, 1996. Detection, mixing, and frequency multiplication of terahertz radiation by two-dimensional electronic fluid. IEEE Trans. Electron Dev. 43, 380–387. https://doi.org/10.1109/16.485650.

[97] L. Vicarelli, M. S. Vitiello, D. Coquillat, et al., 2012. Graphene field-effect transistors as room-temperature terahertz detectors. Nat. Mater. 11, 865. https://doi.org/10.1038/NMAT3417.

[98] D. A. Bandurin, D. Svintsov, I. Gayduchenko, et al., 2018. Resonant terahertz detection using graphene plasmons. Nat.

Commun. 9, 5392. https://doi.org/10.1038/s41467-018-07848-w.

[99] V. V. Popov, O. V. Polischuk, A. R. Davoyan, V. Ryzhii, T. Otsuji, M. S. Shur, 2012. Plasmonic terahertz lasing in an array of graphene nanocavities. Phys. Rev. B 86, 195437. https://doi.org/10.1103/physrevb.86.195437.

[100] Y. Koseki, V. Ryzhii, T. Otsuji, V. V. Popov, and A. Satou, "Giant plasmon instability in a dual-grating-gate graphene field-effect transistor," *Phys. Rev. B*, vol. 93, p. 245408, 2016, https://doi.org/10.1103/PhysRevB.93.245408.

[101] Y. Li and R. Paiella, "Interminiband optical transitions in graphene lateral superlattices," *ACS Photon.*, vol. 5, pp. 3331–3337, 2018, https://doi.org/10.1021/acsphotonics.8b00584.

[102] D. Sun, C. Divin, J. Rioux, et al., 2010. Coherent control of ballistic photocurrents in multilayer epitaxial graphene using quantum interference. Nano Lett. 10, 1293. https://doi.org/10.1021/nl9040737.

[103] L. Prechtel, L. Song, D. Schuh, P. Ajayan, W. Wegscheider, A. W. Holleitner, 2012. Time-resolved ultrafast photocurrents and terahertz generation in freely suspended graphene. Nat. Commun. 3, 646. https://doi.org/10.1038/ncomms1656.

[104] Y. M. Bahk, G. Ramakrishnan, J. Choi, et al., 2014. Plasmon enhanced terahertz emission from single layer graphene. ACS Nano 8, 9089–9096. https://doi.org/10.1021/nn5025237.

[105] H. A. Hafez, S. Kovalev, J. C. Deinert, et al., 2018. Extremely efficient terahertz high-harmonic generation in graphene by hot Dirac fermions. Nature 561, 507–511. https://doi.org/10.1038/s41586-018-0508-1.

[106] P. A. George, J. Strait, J. Dawlaty, et al., 2008. Ultrafast optical-pump terahertz-probe spectroscopy of the carrier relaxation and recombination dynamics in epitaxial graphene. Nano Lett. 8, 4248–4251. https://doi.org/10.1021/nl8019399.

[107] M. Breusing, S. Kuehn, T. Winzer, et al., 2011. Ultrafast nonequilibrium carrier dynamics in a single graphene layer. Phys. Rev. B 83, 153410. https://doi.org/10.1103/PhysRevB.83.153410.

[108] S. Winnerl, M. Orlita, P. Plochocka, et al., 2011. Carrier relaxation in epitaxial graphene photoexcited near the Dirac point. Phys. Rev. Lett. 107, 237401. https://doi.org/10.1103/physrevlett.107.237401.

[109] S. Boubanga-Tombet, S. Chan, T. Watanabe, A. Satou, V. Ryzhii, T. Otsuji, 2012. Ultrafast carrier dynamics and terahertz emission in optically pumped graphene at room temperature. Phys. Rev. B 85, 35443. https://doi.org/10.1103/physrevb.85.035443.

[110] T. Otsuji, S. A. Boubanga Tombet, A. Satou, et al., 2012. Graphene-based devices in terahertz science and technology. J. Phys. D: Appl. Phys. 45, 303001. https://doi.org/10.1088/0022-3727/45/30/303001.

[111] T. Watanabe, T. Fukushima, Y. Yabe, et al., 2013. The gain enhancement effect of surface plasmon polaritons on terahertz stimulated emission in optically pumped monolayer graphene. New J. Phys. 15, 075003. https://doi.org/10.1088/1367-2630/15/7/075003.

[112] T. Yadav, G. Tamamushi, T. Watanabe, et al., 2018. Terahertz light-emitting graphene-channel transistor toward single-mode lasing. Nanophotonics 7, 741–752. https://doi.org/10.1515/nanoph-2017-0106.

[113] R. Kim, V. Perebeinos, P. Avouris, 2011. Relaxation of optically excited carriers in graphene. Phys. Rev. B 84, 075449. https://doi.org/10.1103/PhysRevB.84.075449.

[114] R. R. Nair, P. Blake, A. N. Grigorenko, et al., 2008. Fine structure constant defines visual transparency of graphene. Science 320, 1308. https://doi.org/10.1126/science.1156965.

[115] Y. Li, P. Ferreyra, A. K. Swan, R. Paiella, 2019. Current-driven terahertz light emission from graphene plasmonic oscillations. ACS Photon. 6, 2562–2569. https://doi.org/10.1021/acsphotonics.9b01037.

[116] R. A. Höpfel, E. Vass, E. Gornik, 1982. Thermal excitation of two-dimensional plasma oscillations. Phys. Rev. Lett. 49, 1667–1671. https://doi.org/10.1103/PhysRevLett.49.1667.

[117] K. Hirakawa, K. Yamanaka, M. Grayson, D. C. Tsui, 1995. Far-infrared emission spectroscopy of hot two-dimensional plasmons in Al0.3Ga0.7As/GaAs heterojunctions. Appl. Phys. Lett. 67, 2326–2328. https://doi.org/10.1063/1.114333.

[118] A. Manjavacas, S. Thongrattanasiri, J. J. Greffet, F. J. García de Abajo, 2014. Graphene optical-to-thermal converter. Appl. Phys. Lett. 105, 211102. https://doi.org/10.1063/1.4902429.

[119] M. Freitag, H. Y. Chiu, M. Steiner, V. Perebeinos, P. Avouris, 2010. Thermal infrared emission from biased graphene. Nat. Nanotechnol. 5, 497–501. https://doi.org/10.1038/nnano.2010.90.

[120] V. W. Brar, M. C. Sherrott, M. S. Jang, et al., "Electronic modulation of infrared radiation in graphene plasmonic resonators," *Nat. Commun.*, vol. 6, p. 7032, 2015, https://doi.org/10.1038/ncomms8032.

[121] Y. D. Kim, H. Kim, Y. Cho, et al., "Bright visible light emission from graphene," *Nat. Nanotechnol.*, vol. 10, pp. 676–681, 2015, https://doi.org/10.1038/nnano.2015.118.

[122] I. Kaminer, Y. T Katan, H. Buljan, et al., "Efficient plasmonic emission by the quantum Čerenkov effect from hot carriers in graphene," *Nat. Commun.*, vol. 7, pp. 11880, 2016, https://doi.org/10.1038/ncomms11880.

[123] C. F. Bohren and D. R. Huffman. *Absorption and Scattering of Light by Small Particles*. Chapter 4.7. Weinheim, WileyVCH, 2004.

[124] J. C. W. Song, M. Y. Reizer, L. S. Levitov, 2012. Disorder-assisted electron-phonon scattering and cooling pathways in graphene. Phys. Rev. Lett. 109, 106602. https://doi.org/10.1103/PhysRevLett.109.106602.

[125] M. W. Graham, S. F. Shi, D. C. Ralph, J. Park, P. L. McEuen, 2013. Photocurrent measurements of supercollision cooling in graphene. Nat. Phys. 9, 103–108. https://doi.org/10.1038/NPHYS2493.

[126] A. C. Betz, S. H. Jhang, E. Pallecchi, et al., 2013. Supercollision cooling in undoped graphene. Nat. Phys. 9, 109–112. https://doi.org/10.1038/nphys2494.

[127] U. R. Pfeiffer, R. Jain, J. Grzyb, S. Malz, P. Hillger, and P. Rodríguez-Vízquez, "Current status of terahertz integrated circuits - from components to systems," in *IEEE BiCMOS and Compound Semiconductor Integrated Circuits and Technology Symposium (BCICTS)*, 2018, pp. 1–7.

[128] T. Harter, S. Muehlbrandt, S. Ummethala, et al., "Silicon–plasmonic integrated circuits for terahertz signal generation and coherent detection," *Nat. Photon.*, vol. 12, pp. 625–633, 2018, https://doi.org/10.1038/s41566-018-0237-x.